Tanaka, Y., Klemann, V., Fleming, K., Martinec, Z. (2009): Spectral finite element approach to postseismic deformation in a viscoelastic self-gravitating spherical earth. - Geophysical Journal International, 176, 3, pp. 715—739.

DOI: http://doi.org/10.1111/j.1365-246X.2008.04015.x

Geophys. J. Int. (2009) **176,** 715–739 doi: 10.1111/j.1365-246X.2008.04015.x

Spectral finite element approach to postseismic deformation in a viscoelastic self-gravitating spherical Earth

Y. Tanaka,[1]* V. Klemann,[2] K. Fleming[2] and Z. Martinec[2,3]

[1]*Geographical Survey Institute,* 1, *Kitasato, Tsukuba, Ibaraki,* 305-0811, *Japan. E-mail: y-tanaka@eri.u-tokyo.ac.jp*
[2]*GeoForschungsZentrum Potsdam, Telegrafenberg,* D-14473 *Potsdam, Germany*
[3]*Charles University, V Holešovičkách* 2, 180 00 *Prague* 8, *Czech Republic*

Accepted 2008 October 16. Received 2008 October 16 in original form 2007 October 4

SUMMARY

Theoretical models of the viscoelastic relaxation of a spherical Earth are derived to model large-scale postseismic deformation resulting from great earthquakes ($M > 7$) over decadal timescales. Most existing models of postseismic deformation do not consider strong lateral heterogeneities in mantle viscosity, in particular in the subducting slab where such events occur. In addition, the self-gravitation effect is often treated only approximately. Both effects become important when observations from space geodetic techniques such as GPS and GRACE are interpreted. In this paper, we present a spectral finite-element approach that allows these two effects to be considered in a rigorous way. In this way, much larger lateral viscosity variations can be handled than by perturbation techniques. We derive interface conditions for an arbitrary shear fault in the form of double-couple forces that are equivalent to a prescribed dislocation and simulate a relaxation process for an incompressible Maxwell earth with a 3-D viscoelastic structure. Computational results are validated for a spherically symmetric model by an independent method based on the inverse Laplace integration, and good agreement is obtained. As an example, we apply this approach to the 2004 Sumatra–Andaman earthquake and simulate a large-scale postseismic gravity potential variation by a forward calculation. In the presence of a slab, the secular variation in geoid height change decreases by 30 per cent for wavelengths longer than 500 km, with respect to the case excluding the slab. The effect of the slab can exceed 0.3 mm yr^{-1} for short-term variations when the asthenosphere viscosity is 10^{19} Pa s, which are larger than the observation errors of GRACE. For a displacement field, a decrease in deformation rates can amount to 70 per cent due to the inclusion of a slab, which is detectable with geodetic observations such as GPS. The effect of the slab is attenuated in the gravity field for such longer wavelengths since horizontal scales of the slab are smaller than its spatial resolution. Lateral heterogeneities in viscosity due to a slab should therefore be considered for interpreting observed postseismic relaxation due to a large thrust event in a subduction zone.

Key words: Satellite geodesy; Transient deformation; Seismic cycle; Time variable gravity; Subduction zone processes; Dynamics of lithosphere and mantle.

1 INTRODUCTION

Advanced space geodetic observations such as GPS and GRACE have revealed that the 2004 Sumatra–Andaman earthquake ($M_w = 9.3$; Stein & Okal 2005)) caused crustal movement and gravity variation at spatial scales exceeding 1000 km (Banerjee *et al.* 2005; Han *et al.* 2006; Chen *et al.* 2007; Panet *et al.* 2007). The interpretation of such large-scale deformation requires the application of a theoretical framework that includes the effects of the curvature of the Earth and its self-gravitation (Sun & Okubo 1993; Sun *et al.* 1996; Piersanti *et al.* 1995; Pollitz 1997; Wang 1999; Pollitz 2003; Tanaka *et al.* 2006, 2007). For instance, co- and postseismic crustal movement associated with the Sumatra event has been estimated with spherically symmetric earth models by Boschi *et al.* (2006), Fu & Sun (2006) and Pollitz *et al.* (2006). Piersanti *et al.* (1997) and Piersanti (1999) modelled postseismic deformation caused by the 1964 Alaska and 1960 Chile events, using an

*Now at: Earthquake Research Institute, University of Tokyo, 1-1-1, Yayoi, Bunkyo-ku, Tokyo 113-0032, Japan.

incompressible spherical earth model. The minute coseismic gravity change caused by the 2003 Tokachi–Oki earthquake with $M_w = 8.0$ was detected by a network of superconducting gravimeters, even at an epicentral distance of 1000 km and was successfully reproduced by a theory based on a spherical earth model (Imanishi *et al.* 2004).

Postseismic deformation induced by large earthquakes over decadal timescales is driven by the viscoelastic relaxation of the Earth, reflecting mainly the rheology of the asthenosphere (e.g. Thatcher & Rundle 1979; Fukahata *et al.* 2004; Lorenzo-Martin *et al.* 2006). Most previous theories of viscoelastic postseismic deformation of spherical earth models are based on the normal mode approach (Peltier 1974), assuming radial stratifications of the elastic parameters, density and viscosity. Sabadini *et al.* (1984) calculated perturbations in the moment of inertia induced by posteismic deformation of incompressible earth models. Pollitz (1992) computed surface deformation for a compressible earth model in the absence of self-gravitation. Later, he incorporated the effect of self-gravitation approximately into the formulation, neglecting time variations in the perturbed gravity potential (Pollitz 1997). He also showed that viscoelastic relaxation may account for postseismic deformation caused by local events with shorter timescales (e.g. Pollitz *et al.* 2001). Piersanti *et al.* (1995) derived normal mode solutions for a self-gravitating, incompressible and multilayered earth model. Combining the reciprocity theorem (Okubo 1993) with the normal mode method, Wang (1999) computed vertical deformation in the presence of self-gravitation and compressibility for earth models with a simple viscosity profile. Tanaka *et al.* (2006, 2007), on the other hand, showed that the numerical integration for the inverse Laplace transform is valid for computing relaxation processes of finely stratified, compressible and self-gravitating earth models, without imposing additional constraints on the viscoelastic parameters.

These approaches, however, do not consider the lateral heterogeneities in rheology that occur in plate subduction zones where large earthquakes ($M_w \sim 8$) have frequently occurred. Temperature variations inferred from seismic tomography indicate that a slab has a higher viscosity than the surrounding mantle by several orders of magnitude (e.g. Zhao *et al.* 1994 and Chapters 1.3 and 3.2 in Karato 2003). Nevertheless, only a small number of methods have been proposed for calculating postseismic relaxation of a spherical Earth with a laterally heterogeneous viscosity distribution. Pollitz (2003) developed a semi-analytical approach to take into account laterally heterogeneous elastic parameters and viscosity by applying seismic scattering theory to the normal mode representation established in his previous theory (Pollitz 1997). Finite element methods have also been applied to include the effect of the Earth's curvature and self-gravitation (e.g. Bolte *et al.* 2007). In most previous finite element modelling, however, self-gravitation is not treated as a body force, but its effect is only simulated approximately (e.g. Cohen 1994; Wang *et al.* 2001; Hu *et al.* 2004).

In studies of 'coseismic' deformation, on the other hand, Fu & Sun (2007) applied a perturbation method for tidal deformation to consider global lateral heterogeneities in density for a spherical model. Du *et al.* (1994), later corrected by Cervelli *et al.* (1999), derived a general solution of the elastic response of a laterally heterogeneous half-space medium by using a perturbation method (references describing solutions for particular cases can be also found in the review by Du *et al.* 1994).

The studies dealing with lateral heterogeneities in computations of the viscoelastic response of the Earth to surface loading have the same theoretical framework as that of postseismic relaxation. Several approaches have been developed, including an iterative technique to estimate eigenmode coupling in the Laplace domain (D'Agostino *et al.* 1997), a perturbation method in Cartesian geometry (Kaufmann & Wolf 1999), a perturbation theory making use of the eigenfunction expansion formalism (Tromp & Mitrovica 2000), as well as finite element approaches (e.g. Sabadini *et al.* 1986; Gasperini & Sabadini 1989; Kaufmann *et al.* 1997; Martinec 2000; Zhong *et al.* 2003).

A suitable method for computing the postseismic relaxation of a spherical Earth in the presence of a subducting plate is the spectral finite-element approach (Martinec 2000). This technique was applied by Klemann *et al.* (2007) to model the response of a slab structure to glacial changes in Patagonia, which showed the substantial influence of slab geometry on the induced displacement field. The advantages of this method are (1) the effects of the Earth's curvature and self-gravitation are rigorously treated; (2) the method enables much larger variations in viscosity to be considered than is possible by perturbation methods; (3) the parametrization of stress is based on tensor spherical harmonics, without a need to use the Laplace transform, avoiding coupling between Laplace eigenmodes influenced by different spherical harmonic degrees (e.g. Wu 2002) and (4) the weak formulation used and the finite element representation in the radial direction allows us to treat seismic sources in a more analytical way.

In this study, we apply the spectral finite element approach to viscoelastic deformation caused by an internal dislocation to investigate the effect of a subducting plate on postseismic relaxation in a self-gravitating spherical earth model. In the subsequent section, we explain how to modify the boundary conditions in Martinec (2000), originally formulated for a surface load, to treat an internal dislocation and derive their spectral finite element representation for an arbitrary shear dislocation, including strike-slip and dip-slip components. In Section 3, the derived boundary conditions are validated by an independent method to calculate postseismic relaxation in a spherically symmetric model (Tanaka *et al.* 2006, 2007). In Section 4, postseismic deformation in the presence of a slab is simulated. Effects due to a slab are discussed by comparing the results with those computed for a model excluding the slab. Our conclusions are summarized in Section 5.

2 METHOD

2.1 An outline of the spectral finite element approach for surface loading

In this section, we give an outline of the spectral finite-element approach presented by Martinec (2000), which will be modified to consider postseismic deformations in the same mathematical framework. The governing equations for viscoelastic deformation of an initially

hydrostatically pre-stressed self-gravitating sphere can be written as

$$\mathrm{div}\boldsymbol{\tau} - \rho_0 \mathrm{grad}\phi_1 + \mathrm{div}(\rho_0 \mathbf{u})\mathrm{grad}\phi_0 - \mathrm{grad}(\rho_0 \mathbf{u} \cdot \mathrm{grad}\phi_0) = 0, \tag{1}$$

$$\nabla^2 \phi_1 + 4\pi G \mathrm{div}(\rho_0 \mathbf{u}) = 0 \tag{2}$$

(e.g. Dahlen 1974), where $\mathbf{u}$, ϕ, $\boldsymbol{\tau}$ and G represent the displacement, the gravity potential increment, the stress tensor and Newton's gravitational constant, respectively, $\rho_0 = \rho_0(r)$ is the initial density, r is the radial distance from the centre of the Earth and the hydrostatic and the perturbed states are expressed by the subscripts 0 and 1, respectively. Moreover, the constitutive equations for a Maxwell viscoelastic material and the constraint of incompressibility are written as

$$\dot{\boldsymbol{\tau}} = \dot{\boldsymbol{\tau}}^E - \frac{\mu}{\eta}(\boldsymbol{\tau} - \Pi \boldsymbol{I}), \tag{3}$$

$$\boldsymbol{\tau}^E = \Pi \boldsymbol{I} + 2\mu \boldsymbol{\epsilon}, \tag{4}$$

$$\mathrm{div}\mathbf{u} = 0, \tag{5}$$

where $\boldsymbol{\epsilon} = \frac{1}{2}(\mathrm{grad}\mathbf{u} + \mathrm{grad}^{\mathrm{T}}\mathbf{u})$ is the strain tensor, Π is the pressure increment, $\boldsymbol{I}$ is the second-order identity tensor and the dots denote time derivatives. $\mu = \mu(r)$ denotes the 1-D (spherically symmetric) elastic rigidity and $\eta = \eta(r, \theta, \varphi)$ represents the 3-D viscosity, where θ and φ are colatitude and longitude, respectively.

The boundary conditions are imposed at the Earth's surface and the discontinuity between the mantle and the fluid outer core. At the surface, a surface-mass density and the associated potential discontinuity are given. At the core–mantle boundary, the continuity of the normal component of the displacement and the stress vector, while assuming free-slip behaviour, are employed.

To solve these boundary value problems, a single-level explicit time-differencing scheme is introduced into the time derivative in the constitutive equation (eq. 3), and a finite-element approximation is applied in the radial direction. The angular dependence in the field variables $\mathbf{u}$, ϕ, Π and $\boldsymbol{\epsilon}$ are described by expanding these quantities into spherical harmonics:

$$\mathbf{u}(r, \theta, \varphi) = \sum_{j=0}^{\infty} \sum_{m=-j}^{j} \left[U_{jm}(r)\mathbf{S}_{jm}^{(-1)}(\theta, \varphi) + V_{jm}(r)\mathbf{S}_{jm}^{(1)}(\theta, \varphi) + W_{jm}(r)\mathbf{S}_{jm}^{(0)}(\theta, \varphi) \right], \tag{6}$$

$$\phi_1(r, \theta, \varphi) = \sum_{j=0}^{\infty} \sum_{m=-j}^{j} F_{jm}(r) Y_{jm}(\theta, \varphi), \tag{7}$$

$$\Pi(r, \theta, \varphi) = \sum_{j=0}^{\infty} \sum_{m=-j}^{j} \Pi_{jm}(r) Y_{jm}(\theta, \varphi), \tag{8}$$

$$\boldsymbol{\epsilon}(r, \theta, \varphi) = \sum_{j=0}^{\infty} \sum_{m=-j}^{j} \sum_{\lambda=1}^{6} \epsilon_{jm}^{\lambda}(r) \mathbf{Z}_{jm}^{\lambda}(\theta, \varphi), \tag{9}$$

where $Y_{jm}(\theta, \varphi)$ denotes a scalar spherical harmonic of degree j and order m and $\mathbf{S}_{jm}^{(\lambda)}$, $\lambda = -1, 0, 1$, and $\mathbf{Z}_{jm}^{(\lambda)}$, $\lambda = 1, \ldots, 6$, are vector and tensor spherical harmonics (Martinec 2000), respectively. Their definitions are given in appendix B of Martinec (2000). In eq. (6), terms including U_{jm} and V_{jm} express spheroidal motion and terms including W_{jm} describe toroidal motion. The finite element representation for the radial functions in eqs (6)–(8) can be defined as

$$[U_{jm}(r), V_{jm}(r), W_{jm}(r), F_{jm}(r)] = \sum_{k=1}^{P+1} \left[U_{jm}^k, V_{jm}^k, W_{jm}^k, F_{jm}^k \right] \psi_k(r), \tag{10}$$

where $\psi_k(r) = \frac{r_{k+1} - r}{h_k}$ and $\psi_{k+1}(r) = \frac{r - r_k}{h_k}$ denote the piecewise linear finite elements, and

$$\Pi_{jm}(r) = \sum_{k=1}^{P} \Pi_{jm}^k \xi_k(r), \tag{11}$$

where $\xi_k(r) = 1$ for $r_k \le r \le r_{k+1}$, denotes the piecewise-constant finite elements. Here, $h_k = r_{k+1} - r_k$ and P denotes the number of subintervals on $r_{\mathrm{CMB}} = r_1 < r < r_{P+1} = a$, where r_{CMB} is the radial distance at the core–mantle boundary and a is the radial distance at the Earth's surface.

The solution of the problem, that is, the expansion coefficients of the finite element functions in eqs (10) and (11), are determined so that the following variational equality is satisfied for all test functions, $\delta\mathbf{u}$, $\delta\phi_1$ and $\delta\Pi$, in the same functional space as the solutions $\mathbf{u}^{i+1}$, ϕ_1^{i+1} and Π^{i+1}:

$$\delta\mathcal{E}(\mathbf{u}^{i+1}, \phi_1^{i+1}, \Pi^{i+1}, \delta\mathbf{u}, \delta\phi_1, \delta\Pi) = \delta\mathcal{F}^{i+1}(\delta\mathbf{u}, \delta\phi_1), \tag{12}$$

where i denotes the ith time step, and $\delta\mathcal{E}$ and $\delta\mathcal{F}$ represent the variations of the energy functionals and the variations of the functionals associated with applied forces and viscoelastic dissipation, respectively. The bilinear functional of the solution and the test function on the

left-hand side of eq. (12) are defined as the sum of the variations in the energy associated with the pressure, elastic shear energy, gravitational energy and the term associated with the uniqueness of the solution (Martinec 2000):

$$\delta\mathcal{E}(\mathbf{u}, \phi_1, \Pi, \delta\mathbf{u}, \delta\phi_1, \delta\Pi) = \delta\mathcal{E}_{\text{press}}(\mathbf{u}, \Pi, \delta\mathbf{u}, \delta\Pi) + \delta\mathcal{E}_{\text{shear}}(\mathbf{u}, \delta\mathbf{u}) + \delta\mathcal{E}_{\text{grav}}(\mathbf{u}, \phi_1, \delta\mathbf{u}, \delta\phi_1) + \delta\mathcal{E}_{\text{uniq}}(\mathbf{u}, \delta\mathbf{u}). \tag{13}$$

The linear functional at the right-hand side of eq. (12) is defined as

$$\delta\mathcal{F}^{i+1}(\delta\mathbf{u}, \delta\phi_1) = \delta\mathcal{F}^{i}_{\text{diss}}(\delta\mathbf{u}) + \delta\mathcal{F}^{i+1}_{\text{surf}}(\delta\mathbf{u}, \delta\phi_1) + \delta\mathcal{W}^{i+1}(\delta\mathbf{u}, \delta\phi_1). \tag{14}$$

Here, $\delta\mathcal{F}^{i+1}_{\text{surf}}$ in eq. (14) represents the functional related to a prescribed surface load and can be specifically written as

$$\mathcal{F}^{i+1}_{\text{surf}} = \int \left(\mathbf{b}_0^{i+1} \cdot \mathbf{u} + \mathrm{b}_1^{i+1}\phi_1\right) \mathrm{d}S, \tag{15}$$

$$\mathbf{b}_0^{i+1} = -[\mathbf{e}_r \cdot \boldsymbol{\tau}^{\boldsymbol{i+1}}]^+_- = -g_0(r = a)\sigma^{i+1}\mathbf{e}_r, \tag{16}$$

$$\begin{aligned} b_1^{i+1} &= -\left[\left(\mathrm{grad}\phi_1^{i+1} + 4\pi G\rho_0\mathbf{u}^{i+1}\right) \cdot \mathbf{e}_r\right]^+_- \\ &= -\frac{1}{4\pi G}\frac{j+1}{a}\phi_1^{i+1} - \sigma^{i+1}, \end{aligned} \tag{17}$$

where d S denotes the element of the external surface with radius $r = a$ and $\mathbf{e}_r$, σ and g_0 are the unit normal vector, the surface mass-load density and the unperturbed gravity, respectively. $\delta\mathcal{W}^{i+1}$ denotes the variation of the work done by the applied internal forces, which does not appear for the case of surface loading but will be introduced in Section 2.2 when postseismic deformation is discussed. $\delta\mathcal{F}^{i}_{\text{diss}}$ is the variation of the dissipative energy defined as $[-\int(\boldsymbol{\tau}^{V,i}\delta\boldsymbol{\epsilon})\mathrm{d}V]$, which can be evaluated by the volume integration of the product of the non-elastic part of the stress tensor computed for the displacement at the previous time step i and the strain calculated for the test function. By this term, coupling effects between the spheroidal and toroidal deformation due to lateral heterogeneity in viscosity are taken into account. The other terms in eq. (12) are evaluated at the current time step $(i + 1)$, meaning the solution at the current time can be recursively determined once an initial value is given. Consequently, the solution is obtained such that the difference of the energy caused by the deformation $(= \mathcal{E})$ from the sum of the energy generated by the boundary conditions and the dissipated energy $(= \mathcal{F})$ takes a stationary value at each time step $[\delta(\mathcal{E} - \mathcal{F}) = 0]$. Considering that eq. (12) holds for all $\delta\mathbf{u}$, $\delta\phi_1$ and $\delta\Pi$, it is finally reduced to the form of the following linear algebraic equation:

$$\mathbf{A}\mathbf{x}^{i+1} = \mathbf{f}^{i+1}, \mathbf{f}^{i+1} = \mathbf{f}^{i+1}\left(\mathbf{b}_0^{i+1}, {b_1}^{i+1}, \mathbf{x}^{i}\right), \tag{18}$$

where $\mathbf{x}^{i+1}$ denotes the solution vector at the current time $(i + 1)$ and $\mathbf{A}$ is the time-independent matrix, whose expression is explicitly given in Martinec (2000) and $\mathbf{b}_0^{i+1}$, b_1^{i+1} and $\mathbf{x}^0$ are the prescribed boundary and initial conditions.

2.2 Spectral finite element description of the source conditions

The governing equations for viscoelastic deformation caused by a dislocation in an initially hydrostatic, self-gravitating and incompressible spherical Earth have exactly the same forms as eqs (1)–(5) (e.g. Piersanti *et al.* 1995). Therefore, by specifying the appropriate interface conditions corresponding to postseismic deformation, we can use the spectral finite element approach in computations of postseismic relaxation.

2.2.1 Boundary conditions for postseismic relaxation

Boundary conditions for postseismic deformation are imposed at the Earth's surface $(r = a)$, a seismic source and the core–mantle boundary. The free surface condition is constituted by setting the surface-mass density to zero in eqs (16) and (17):

$$\boldsymbol{\tau} \cdot \mathbf{e}_r = 0, \tag{19}$$

$$(\mathrm{grad}\phi_1^{\text{ext}} - \mathrm{grad}\phi_1 - 4\pi G\rho_0\mathbf{u}) \cdot \mathbf{e}_r = 0, \tag{20}$$

$$\mathrm{grad}\phi_1^{\text{ext}} = -\frac{j+1}{a}\phi_1, \tag{21}$$

which agrees with the corresponding surface condition for postseismic deformation (e.g. Sun & Okubo 1993). Here, ϕ_1^{ext} is the perturbation of the gravitational potential on the exterior side of the surface (Martinec 2000). The dislocation condition across a fault surface can be written as (Dahlen 1972)

$$[\mathbf{u}]^+_- = \Delta\mathbf{u}, \tag{22}$$

$$[\phi_1]^+_- = 0, \tag{23}$$

$$[\mathbf{n} \cdot \boldsymbol{\tau}]^+_- = \nabla_\Sigma \cdot ([\mathbf{u}]^+_-\mathbf{n} \cdot \boldsymbol{\tau}), \tag{24}$$

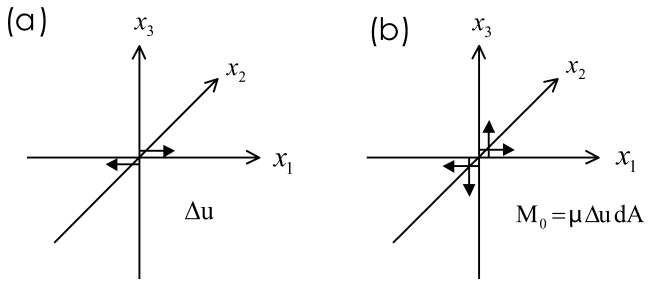

Figure 1. (a) A prescribed dislocation. (b) The equivalent double-couple forces. The same as fig. 4 in Dahlen (1972).

$$[(\mathrm{grad}\phi_1 + 4\pi G\rho_0[\mathbf{u}]^+_-) \cdot \mathbf{n}]^+_- = 0, \tag{25}$$

where $\Delta\mathbf{u}$, $\mathbf{n}$ and $\nabla_\Sigma \equiv \nabla - \mathbf{n}(\mathbf{n} \cdot \nabla)$ denote a prescribed dislocation vector, the unit vector normal to the fault plane Σ and the surface gradient operator on Σ, respectively. The constraint at the core–mantle boundary is the solid–liquid condition, as in the case of surface loading.

2.2.2 How to incorporate the dislocation condition into the presented method?

The split-node technique (Melosh & Raefsky 1981) has been often used to consider a dislocation condition when co- and postseismic deformations are modelled by a finite element method, (e.g. Suito & Hirahara 1999; Hu *et al.* 2004). A merit of this technique is that the formulation of the boundary condition applies neither net forces nor moments to a finite element grid (Melosh & Raefsky 1981). We do not, however, use this technique, since the formulation becomes much more complex and computationally expensive. In the spectral finite element approach followed in this work, the finite elements are introduced in the radial coordinate only. Therefore, when a dislocation is considered across a vertical fault along a latitude line, for instance, the integration domains over the angular variable θ must be divided into two regions, $0 \le \theta \le \theta_0$ and $\theta_0 \le \theta \le \pi$, where θ_0 denotes colatitude at which a source is located. This division breaks the orthogonality of the spherical harmonics when deriving the equation of the energy variation (eq. 12) and reduces computational efficiency.

To consider the dislocation conditions (eqs 22–25), we apply equivalent double-couple forces (e.g. Dahlen 1972). That is, the effect of a prescribed displacement discontinuity across a fault surface is exactly the same as the effect of a hypothetically introduced extra body force into a fault-free medium (Dahlen 1972). The derivation of the equivalent forces is described in the same paper (Dahlen 1972). We take an example of equivalent double-couple forces for an infinitesimal fault surface in an isotropic and initially hydrostatically pre-stressed elastic medium, a fault normal to the direction of the x_2 axis and the dislocation vector parallel with x_1 in a Cartesian axis system x_1, x_2, x_3 (Fig. 1). Then, the equivalent forces are defined as

$$f_1(\mathbf{r}) = -M_0\delta(x_1)\delta(x_2)\frac{\mathrm{d}}{\mathrm{d}x_3}\delta(x_3), \tag{26}$$

$$f_2(\mathbf{r}) = 0, \tag{27}$$

$$f_3(\mathbf{r}) = -M_0\delta(x_2)\delta(x_3)\frac{\mathrm{d}}{\mathrm{d}x_1}\delta(x_1), \tag{28}$$

$$M_0 = \mu(r)\Delta u \mathrm{d}A, \tag{29}$$

where $\mathbf{r} = (x_1, x_2, x_3)$ and $\mathrm{d}A$, Δu and M_0 are the area of an infinitesimal fault surface, a prescribed slip and the moment magnitude, respectively, and $\delta(x_i)$ is the Dirac's delta function. The expressions of the equivalent forces for more general cases can be found in Dahlen (1972).

The advantage of applying equivalent forces is that it is not necessary to perform the division of the integration domain with respect to colatitude θ and longitude φ, which originates from the split-node technique. Instead, new variables $\mathbf{b}_0$, representing the equivalent forces, are introduced in the variation of the linear functional $\delta\mathcal{W}$ in the last term of eq. (14). The angular dependence of equivalent forces is then expanded in terms of vector spherical harmonics, similar to that used in eq. (6). This reduces net forces and moments caused by equivalent forces given on the horizontal surface of $r = r_s$, where $r = r_s$ is the radial distance to the source, compared with the case in which equivalent forces are applied to finite elements deployed along the horizontal direction. As a consequence, effects due to net forces and moments on computational results become sufficiently small (Section 3). In addition, the net force and moment summed over the whole Earth affect deformations of spherical degrees 0 and 1 only, which can be neglected in practice.

2.3 Expressions of boundary conditions using double-couple forces for various sources

We now derive the boundary conditions for all types of shear faults, including strike-slip and dip-slip mechanisms.

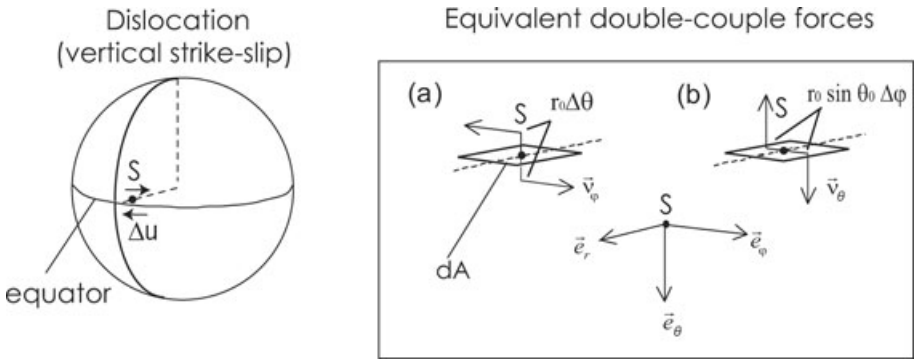

Figure 2. Vertical strike-slip dislocation located below the equator and equivalent double-couple forces to the dislocation (arrows in the right-hand box). Δu denotes the prescribed slip at the source, S, and the fault strike is eastward. $\vec{\mathbf{e}}_r$, $\vec{\mathbf{e}}_\theta$ and $\vec{\mathbf{e}}_\varphi$ are the unit base vectors at S, and (a) and (b) show the single-couple forces forming the double-couple forces. The fault plane with an infinitesimal area is marked by d A. The direction of the single-couple forces (a) is parallel to the fault plane and is the same as that of the dislocation (represented by $\pm\vec{\nu}_\varphi$). The conjugate single-couple forces (b) have a direction perpendicular to the fault, but the moment is opposite to that of the single-couple forces (a) so that the sum of the two moments vanishes (denoted by $\pm\vec{\nu}_\theta$).

2.3.1 Vertical strike-slip fault

We first derive double-couple forces for a vertical strike-slip fault. Fig. 2 depicts a configuration of this problem in the conventional spherical coordinate system, whose unit base vectors are $\mathbf{e}_r$, $\mathbf{e}_\theta$ and $\mathbf{e}_\varphi$. We assume a point dislocation along the direction of $\pm\mathbf{e}_\varphi$ located at $(\theta_0 = \frac{\pi}{2}, \varphi_0 = 0)$. The equivalent double-couple forces at the source are drawn in the figure. They consist of (1) the single-couple forces in the direction of $\pm\mathbf{e}_\varphi$ parallel to the fault and (2) the conjugate single-couple forces in the direction of $\pm\mathbf{e}_\theta$ perpendicular to the plane with $\varphi = \varphi_0$.

The double-couple forces equivalent to the point dislocation are expressed by combining point forces expanded on a sphere. A point force with a unit magnitude applied at $(r_0, \theta_0, \varphi_0)$ can be written in terms of vector spherical harmonics, $\mathbf{S}_{jm}^{(\lambda)}$, as

$$\begin{aligned}\mathbf{f}(r,\theta,\varphi) = \frac{\delta(r-r_0)}{r_0^2}\sum_{j,m}\Bigg\{&\nu_r Y_{jm}^*(\theta,\varphi)|_{\theta_0,\varphi_0}\mathbf{S}_{jm}^{(-1)}(\theta,\varphi)\\ &+\left[\nu_\theta\frac{\partial Y_{jm}^*(\theta,\varphi)}{\partial\theta}+\nu_\varphi\frac{1}{\sin\theta}\frac{\partial Y_{jm}^*(\theta,\varphi)}{\partial\varphi}\right]_{\theta_0,\varphi_0}\mathbf{S}_{jm}^{(1)}(\theta,\varphi)\\ &+\left[-\nu_\theta\frac{1}{\sin\theta}\frac{\partial Y_{jm}^*(\theta,\varphi)}{\partial\varphi}+\nu_\varphi\frac{\partial Y_{jm}^*(\theta,\varphi)}{\partial\theta}\right]_{\theta_0,\varphi_0}\mathbf{S}_{jm}^{(0)}(\theta,\varphi)\Bigg\}\end{aligned} \tag{30}$$

(eq. 257 in Takeuchi & Saito 1972). Here, ν_r, ν_θ and ν_φ represent the three components of the unit direction vector of the prescribed force, **f**, at $\theta = \theta_0$, $\varphi = \varphi_0$ and the asterisk denotes complex conjugate. After substituting $(\nu_r, \nu_\theta, \nu_\varphi) = (0, 0, \pm 1)$ into eq. (30), point forces forming the single-couple forces (1) given at the southern and northern sides of the fault, $\theta = \theta_0 \pm \frac{\Delta\theta}{2}$, can be represented as

$$\begin{aligned}\mathbf{f}^{\theta_0\pm}(r,\theta,\varphi) = \pm\frac{\delta(r-r_0)}{r_0^2}\sum_{j,m}\Bigg\{&\left[\frac{1}{\sin\theta}\frac{\partial Y_{jm}^*(\theta,\varphi)}{\partial\varphi}\right]_{\theta_0\pm\frac{\Delta\theta}{2},\varphi_0}\\ &\times\mathbf{S}_{jm}^{(1)}(\theta,\varphi)+\left[\frac{\partial Y_{jm}^*(\theta,\varphi)}{\partial\theta}\right]_{\theta_0\pm\frac{\Delta\theta}{2},\varphi_0}\mathbf{S}_{jm}^{(0)}(\theta,\varphi)\Bigg\},\end{aligned} \tag{31}$$

where r_0 denotes the radial distance of the point source. We substitute these two forces into the boundary functional $\mathbf{b}_0 \equiv -[\tau\cdot\mathbf{e}_r]_-^+$ and compute the variation of the work due to the applied body forces:

$$\delta\mathcal{W} = \int\mathbf{b}_0\cdot\delta\mathbf{u}\mathrm{d}S = -\int[\boldsymbol{\tau}\cdot\mathbf{e}_r]_-\cdot\delta\mathbf{u}\mathrm{d}S = \int(\mathbf{f}^{\theta_0+}+\mathbf{f}^{\theta_0-})\cdot\delta\mathbf{u}\mathrm{d}S. \tag{32}$$

Here, we applied the forces at the minus side of dS. The integration in eq. (32) is carried out on the spherical surface at radius r_0 (i.e. $\mathrm{d}S = r_0^2\sin\theta\mathrm{d}\theta\mathrm{d}\varphi$). When the moment magnitude is $M_0 \equiv \mu(r_0)\Delta u\,\mathrm{d}A$, where Δu and dA denote the prescribed slip and an infinitesimal area of the fault, respectively, the magnitude of these forces can be represented in terms of the length of the moment arm Δl as

$$\frac{M_0}{\Delta l} = \frac{M_0}{r_0\Delta\theta}. \tag{33}$$

Performing the integration over the angular variable in eq. (32), multiplying the result by $\frac{M_0}{\Delta l}$ and taking the limit of $\Delta\theta\to 0$ as $M_0 =$ constant, we obtain

$$\begin{aligned}\delta\mathcal{W} &= \delta(r-r_0)\sum_{j,m}\left[\left\{\frac{\partial}{\partial\theta}\left[\frac{1}{\sin\theta}\frac{\partial Y_{jm}^*(\theta,\varphi)}{\partial\varphi}\right]\right\}_{\theta_0,\varphi_0}\delta V_{jm}+\left[\frac{\partial^2 Y_{jm}^*(\theta,\varphi)}{\partial\theta^2}\right]_{\theta_0,\varphi_0}\delta W_{jm}\right]\Delta\theta\frac{M_0}{r_0\Delta\theta}\\ &= \delta(r-r_0)\sum_{j,m}\left[\left\{\frac{\partial}{\partial\theta}\left[\frac{1}{\sin\theta}\frac{\partial Y_{jm}^*(\theta,\varphi)}{\partial\varphi}\right]\right\}_{\theta_0,\varphi_0}\delta V_{jm}+\left[\frac{\partial^2 Y_{jm}^*(\theta,\varphi)}{\partial\theta^2}\right]_{\theta_0,\varphi_0}\delta W_{jm}\right]\frac{\mu(r_0)\Delta u\mathrm{d}A}{r_0}.\end{aligned} \tag{34}$$

Similarly, substituting $(\nu_r, \nu_\theta, \nu_\varphi) = (0, \pm 1, 0)$ into eq. (30), point forces forming the conjugate single-couple forces (b) given at $\varphi = \varphi_0 \pm \frac{\Delta\varphi}{2}$, can be represented as

$$\mathbf{f}^{\varphi_0\pm}(r,\theta,\varphi) = \pm\frac{\delta(r-r_0)}{r_0^2}\sum_{j,m}\left\{\left[\frac{\partial Y^*_{jm}(\theta,\varphi)}{\partial\theta}\right]_{\theta_0,\varphi_0\pm\frac{\Delta\varphi}{2}}\mathbf{S}^{(1)}_{jm}(\theta,\varphi) + \left[-\frac{1}{\sin\theta}\frac{\partial Y^*_{jm}(\theta,\varphi)}{\partial\varphi}\right]_{\theta_0,\varphi_0\pm\frac{\Delta\varphi}{2}}\mathbf{S}^{(0)}_{jm}(\theta,\varphi)\right\}. \tag{35}$$

The magnitude of these forces is

$$\frac{M_0}{\Delta l} = \frac{M_0}{r_0\sin\theta_0\Delta\varphi} \tag{36}$$

(Fig. 2). Substituting these forces into $\mathbf{f}^{\theta_0\pm}$ in eq. (32) and following the same procedure to derive eq. (34), the variation of the work due to the conjugate forces can be written as

$$\delta\mathcal{W} = \delta(r-r_0)\sum_{j,m}\left\{\left[\frac{1}{\sin\theta}\frac{\partial^2 Y^*_{jm}(\theta,\varphi)}{\partial\varphi\partial\theta}\right]_{\theta_0,\varphi_0}\delta V_{jm} + \left[-\frac{1}{\sin\theta^2}\frac{\partial^2 Y^*_{jm}(\theta,\varphi)}{\partial\varphi^2}\right]_{\theta_0,\varphi_0}\delta W_{jm}\right\}\frac{\mu(r_0)\Delta u\mathrm{d}A}{r_0}. \tag{37}$$

Finally, taking the sum of eqs (34) and (37) and integrating the result over an incremental area that includes the source ($r = r_0$), we obtain an expression of the energy variation for the source with a unit area:

$$\delta\mathcal{W} = \delta\mathcal{W}^{(\mathrm{E})} + \delta\mathcal{W}^{(\mathrm{ET})}, \tag{38}$$

$$\delta\mathcal{W}^{(E)} = \frac{\mu_k\Delta u\Delta A}{r_0}\sum_{j}^{j_{max}}\sum_{m=-j}^{j}\left\{\frac{1}{\sin\theta}\frac{\partial^2 Y^*_{jm}(\theta,\varphi)}{\partial\theta\partial\varphi} + \frac{\partial}{\partial\theta}\left[\frac{1}{\sin\theta}\frac{\partial Y^*_{jm}(\theta,\varphi)}{\partial\varphi}\right]\right\}_{\theta_0,\varphi_0}\delta V^k_{jm}, \tag{39}$$

$$\delta\mathcal{W}^{(ET)} = \frac{\mu_k\Delta u\Delta A}{r_0}\sum_{j}^{j_{max}}\sum_{m=-j}^{j}\left[\frac{\partial^2 Y^*_{jm}(\theta,\varphi)}{\partial\theta^2} - \frac{1}{\sin^2\theta}\frac{\partial^2 Y^*_{jm}(\theta,\varphi)}{\partial\varphi^2}\right]_{\theta_0,\varphi_0}\delta W^k_{jm}, \tag{40}$$

where $\Delta A = 1$ and j_{max} is a cut-off degree of representation (6), and the superscript k at δV^k_{jm} and δW^k_{jm} indicates that $\delta\mathcal{W}$ is applied at the kth element on the right-hand side in eq. (18), that is, for $r_0 = r_k$. The superscripts (E) associated with the spheroidal motion and (ET) related to the toroidal motion after $\delta\mathcal{W}$ are introduced for later convenience. For time index $i > 0$, eq. (38) must be multiplied by $\exp[-(\mu_k/\eta_k)\mathrm{i}\Delta t]$, where Δt denotes a prescribed time step in the time-difference scheme, otherwise the double-couple forces would be constant over time, consequently increasing the resulting dislocation for a Maxwell viscoelastic body.

The summation over j in eqs (39) and (40) starts from $j = 1$ because the deformation for $j = 0$ is not induced when incompressibility is assumed (Martinec 2000). For $j \geq 1$, the following relationship holds

$$\int\mathbf{S}^{(\lambda)}_{jm}\mathrm{d}\Omega = \sqrt{\frac{4\pi}{3}}\delta_{\mathrm{j1}}(\delta_{\lambda,-1} + 2\delta_{\lambda,1})\mathbf{e}_m, \tag{41}$$

where $\mathbf{e}_m = \mathbf{e}_z, -\frac{1}{\sqrt{2}}(\mathbf{e}_x + \mathrm{i}\mathbf{e}_y), \frac{1}{\sqrt{2}}(\mathbf{e}_x - \mathrm{i}\mathbf{e}_y)$ for $m = 0, 1, -1$, respectively, where i denotes the imaginary number (eq. B7 in Martinec 2000). As a result, the net force and the net torque over the entire sphere occur for $j = 1$. To be specific, the net force can be written as

$$\mathbf{F} \equiv \sum_i\int\mathbf{f}_i\mathrm{d}\Omega = \int\left[(\mathbf{f}^{\theta_0+} + \mathbf{f}^{\theta_0-})\frac{M_0}{r_0\Delta\theta} + (\mathbf{f}^{\varphi_0+} + \mathbf{f}^{\varphi_0-})\frac{M_0}{r_0\sin\theta\Delta\varphi}\right]\mathrm{r}^2\sin\theta\mathrm{d}\theta\mathrm{d}\varphi. \tag{42}$$

Substituting eqs (31) and (35) into eq. (42) and using the relationship of eq. (41), we have

$$\mathbf{F} = M_0\frac{\delta(r-r_0)}{r_0}\sum_{j,m}\left[\frac{\partial}{\partial\theta}\left(\frac{1}{\sin\theta}\frac{\partial Y^*_{jm}}{\partial\varphi}\right) + \frac{1}{\sin\theta}\frac{\partial^2 Y^*_{jm}}{\partial\varphi\partial\theta}\right]_{\theta_0,\varphi_0}\int\mathbf{S}^{(1)}_{jm}\mathrm{d}\Omega = -2M_0\frac{\delta(r-r_0)}{r_0}\frac{1}{\tan\theta_0}(\sin\varphi_0\mathbf{e}_x + \cos\varphi_0\mathbf{e}_y). \tag{43}$$

The net torque, on the other hand, can be defined as

$$\mathbf{N} \equiv \sum_i\int(\mathbf{r}_i\times\mathbf{f}_i)\mathrm{d}\Omega = \int\mathbf{r}_0\times\left[(\mathbf{f}^{\theta_0+} + \mathbf{f}^{\theta_0-})\frac{M_0}{r_0\Delta\theta} + (\mathbf{f}^{\varphi_0+} + \mathbf{f}^{\varphi_0-})\frac{M_0}{r_0\sin\theta\Delta\varphi}\right]\mathrm{r}^2\sin\theta\mathrm{d}\theta\mathrm{d}\varphi, \tag{44}$$

which remains for the toroidal forces of $j = 1$, since

$$\int\mathbf{r}\times\mathbf{S}^{(-1)}_{jm}\mathrm{d}\Omega = \int\mathbf{r}\times\mathbf{S}^{(1)}_{jm}\mathrm{d}\Omega = 0, \tag{45}$$

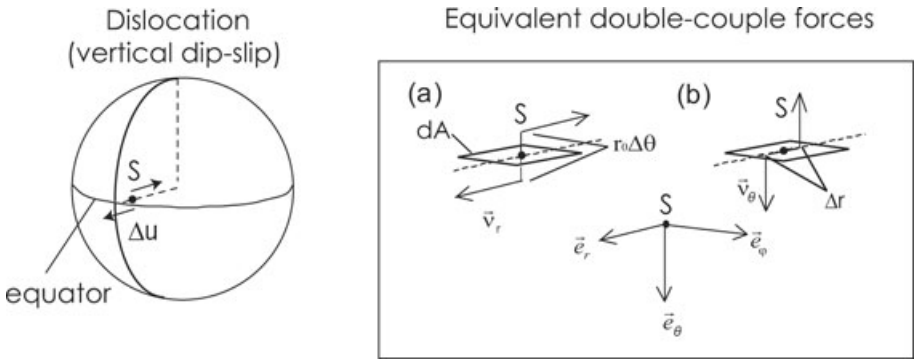

Figure 3. Vertical dip-slip dislocation located below the equator and equivalent double-couple forces to the dislocation. For details, see the caption of Fig. 2.

$$\int \mathbf{r} \times \mathbf{S}^{(0)}_{jm} \mathrm{d}\Omega = -r \int \mathbf{S}^{(1)}_{jm} \mathrm{d}\Omega = -2\sqrt{\frac{4\pi}{3}} r \delta_{j1} \mathbf{e}_m. \tag{46}$$

Substituting eqs (31) and (35) into eq. (44) and using eqs (45) and (46), the net torque finally becomes

$$\begin{aligned} \mathbf{N} &= -M_0 \delta(r - r_0) \sum_{j,m} \left[\frac{\partial^2 Y^*_{jm}}{\partial \theta^2} - \frac{1}{\sin\theta^2} \frac{\partial^2 Y^*_{jm}}{\partial \varphi^2} \right]_{\theta_0, \varphi_0} \int \mathbf{S}^{(1)}_{jm} \mathrm{d}\Omega \\ &= 2M_0 \delta(r - r_0) \left[\cos\theta_0 \mathbf{e}_z + \frac{\cos\theta_0}{\tan\theta_0} (-\cos\varphi_0 \mathbf{e}_x + \sin\varphi_0 \mathbf{e}_y) \right]. \end{aligned} \tag{47}$$

The above net force and net torque, however, causes no translation and rotation of the entire sphere since the uniqueness of the solution is guaranteed by the last term in eq. (13). It is also known that the deformation for $j = 1$ excited in a laterally homogeneous earth model is negligibly small in the total deformation (Sun & Okubo 1993). In a practical computation, therefore, we may neglect the terms with $j = 1$ as long as inhomogeneous viscosity structures with such a long wavelength (20 000 km) are not considered.

Since a slip on a shear fault does not change gravitation, the boundary term b_1 in eq. (17) vanishes and the boundary condition eq. (25) is satisfied identically.

2.3.2 Vertical dip-slip fault

Next, we consider a vertical dip-slip fault (Fig. 3). In this case, the two single-couple forces illustrated in panels (a) and (b) are considered. The single-couple forces (Fig. 3a) can be written by substituting $(\nu_\mathrm{r}, \nu_\theta, \nu_\varphi) = (\pm 1, 0, 0)$ into eq. (30) and replacing θ_0 by $\theta_0 \pm \frac{\Delta\theta}{2}$,

$$\mathbf{f}^{\theta_0 \pm}(r, \theta, \varphi) = \pm \frac{\delta(r - r_0)}{r_0^2} \sum_{j,m} [Y^*_{jm}(\theta, \varphi)]_{\theta_0 \pm \frac{\Delta\theta}{2}, \varphi_0} \mathbf{S}^{(-1)}_{jm}(\theta, \varphi). \tag{48}$$

Following the same procedure as in the strike-slip case, we obtain the expression for the variation of the work as

$$\delta \mathcal{W}^{(\mathrm{B})} = \frac{\mu_k \Delta u \Delta A}{r_0} \sum_{j}^{j_{max}} \sum_{m=-j}^{j} \left[\frac{\partial Y^*_{jm}(\theta, \varphi)}{\partial \theta} \right]_{\theta_0, \varphi_0} \delta U^k_{jm}. \tag{49}$$

The label (B) is introduced for later convenience.

For the conjugate single-couple forces (2), we place the forces in the direction of $\pm \mathbf{e}_\theta$ at different depths ($r = r_{k+1}, r_{k-1}$) to approximate the derivative of the δ function with respect to r (see eq. 26). These forces can be written as

$$\begin{aligned} \mathbf{f}^{r\pm}(r, \theta, \varphi) = \pm \frac{\delta(r - r_{k\pm1})}{r_0^2} \sum_{j,m} \Bigg\{ &\left[\frac{\partial Y^*_{jm}(\theta, \varphi)}{\partial \theta} \right]_{\theta_0, \varphi_0} \mathbf{S}^{(1)}_{jm}(\theta, \varphi) \\ &+ \left[-\frac{1}{\sin\theta} \frac{\partial Y^*_{jm}(\theta, \varphi)}{\partial \varphi} \right]_{\theta_0, \varphi_0} \mathbf{S}^{(0)}_{jm}(\theta, \varphi) \Bigg\}. \end{aligned} \tag{50}$$

Multiplying the magnitude of these forces by

$$\frac{M_0}{\Delta l} = \frac{M_0}{r_{k+1} - r_{k-1}}, \tag{51}$$

we obtain

$$\begin{aligned} \delta \mathcal{W}^{\pm} = \pm \delta(r - r_{k\pm1}) \frac{M_0}{r_{k+1} - r_{k-1}} \sum_{j,m} \Bigg\{ &\left[\frac{\partial Y^*_{jm}(\theta, \varphi)}{\partial \theta} \right]_{\theta_0, \varphi_0} \delta V^{k\pm1}_{jm}(\theta, \varphi) \\ &+ \left[-\frac{1}{\sin\theta} \frac{\partial Y^*_{jm}(\theta, \varphi)}{\partial \varphi} \right]_{\theta_0, \varphi_0} \delta W^{k\pm1}_{jm}(\theta, \varphi) \Bigg\}. \end{aligned} \tag{52}$$

We should note that in this expression, the forces of the same magnitude are prescribed at two different depths, causing a net torque in the spectral domain with respect to $\mathbf{r} = 0$. To correctly consider the effect of the dislocation, torques generated by the applied two forces must balance. To achieve this, we multiply the magnitude of the force applied at r_{k+1} by the factor $\frac{r_k}{r_{k+1}}$ and that applied at r_{k-1} by $\frac{r_k}{r_{k-1}}$. Without introducing these factors, a difference in displacement will increase over time, and reach approximately 10 per cent at the fluid limit.

Finally, substituting $M_0 = \mu(r_k)\Delta u \mathrm{d}A$ into eq. (52) and integrating the result over a small area that includes the source, we obtain the variations of the work for a vertical dip-slip fault with a unit area that are applied at the $(k+1)$th and $(k-1)$th elements:

$$\delta\mathcal{W}^{\|+1} \equiv \delta\mathcal{W}^{(\mathrm{D}+)} + \delta\mathcal{W}^{(\mathrm{D}+\mathrm{T})}, \tag{53}$$

$$\delta\mathcal{W}^{(D+)} = \frac{\mu_k \Delta u \Delta A}{r_0} \frac{r_k}{r_{k+1} - r_{k-1}} \left(\frac{r_k}{r_{k+1}}\right) \sum_{j,m} \left[\frac{\partial Y^*_{jm}(\theta,\varphi)}{\partial\theta}\right]_{\theta_0,\varphi_0} \delta V^{k+1}_{jm}, \tag{54}$$

$$\delta\mathcal{W}^{(D+T)} = -\frac{\mu_k \Delta u \Delta A}{r_0} \frac{r_k}{r_{k+1} - r_{k-1}} \left(\frac{r_k}{r_{k+1}}\right) \sum_{j,m} \left[\frac{1}{\sin\theta}\frac{\partial Y^*_{jm}(\theta,\varphi)}{\partial\varphi}\right]_{\theta_0,\varphi_0} \delta W^{k+1}_{jm}, \tag{55}$$

$$\delta\mathcal{W}^{\|-1} \equiv \delta\mathcal{W}^{(\mathrm{D}-)} + \delta\mathcal{W}^{(\mathrm{D}-\mathrm{T})}, \tag{56}$$

$$\delta\mathcal{W}^{(D-)} = -\frac{\mu_k \Delta u \Delta A}{r_0} \frac{r_k}{r_{k+1} - r_{k-1}} \left(\frac{r_k}{r_{k-1}}\right) \sum_{j,m} \left[\frac{\partial Y^*_{jm}(\theta,\varphi)}{\partial\theta}\right]_{\theta_0,\varphi_0} \delta V^{k-1}_{jm}, \tag{57}$$

$$\delta\mathcal{W}^{(D-T)} = \frac{\mu_k \Delta u \Delta A}{r_0} \frac{r_k}{r_{k+1} - r_{k-1}} \left(\frac{r_k}{r_{k-1}}\right) \sum_{j,m} \left[\frac{1}{\sin\theta}\frac{\partial Y^*_{jm}(\theta,\varphi)}{\partial\varphi}\right]_{\theta_0,\varphi_0} \delta W^{k-1}_{jm}. \tag{58}$$

The equivalent forces for $j = 1$ may be neglected for the same reason as for the strike-slip case.

2.3.3 Shear fault

We consider a shear fault with dip and rake angles of δ and α, respectively (Fig. 4). In this case, equivalent double-couple forces can be decomposed into the following six components. First, Figs 5(A)–(D) show four types of 'single'-couple forces associated with a dislocation in the dip direction. The corresponding double-couple forces can be obtained by subtracting the expressions for the dip angle of $\delta + \pi/2$ from those for δ. In the previous section, we have derived the expressions for single-couple forces Figs 5(B) and (D) (vertical dip-slip). The representations of Figs 5(A) and (C) are obtained by changing the direction of the applied forces by $\pi/2$. Considering the contributions from the conjugate single-couple forces, the variation of the work for the spheroidal components can be written as

$$\delta\mathcal{W}^{(A)} = -\frac{\mu_k \Delta u \Delta A}{r_0} \sin 2\delta \sin\alpha \sum_{j,m} \left[\frac{\partial^2 Y^*_{jm}(\theta,\varphi)}{\partial\theta^2}\right]_{\theta_0,\varphi_0} \delta V^k_{jm}, \tag{59}$$

$$\delta\mathcal{W}^{(B)} = -\frac{\mu_k \Delta u \Delta A}{r_0} \cos 2\delta \sin\alpha \sum_{j,m} \left[\frac{\partial Y^*_{jm}(\theta,\varphi)}{\partial\theta}\right]_{\theta_0,\varphi_0} \delta U^k_{jm}, \tag{60}$$

$$\delta\mathcal{W}^{(C+)} = \frac{\mu_k \Delta u \Delta S}{r_0} \sin 2\delta \sin\alpha \frac{r_k}{r_{k+1} - r_{k-1}} \left(\frac{r_k}{r_{k+1}}\right) \sum_{j,m} Y_{jm}(\theta,\varphi)^*|_{\theta_0,\varphi_0} \delta U^{k+1}_{jm}, \tag{61}$$

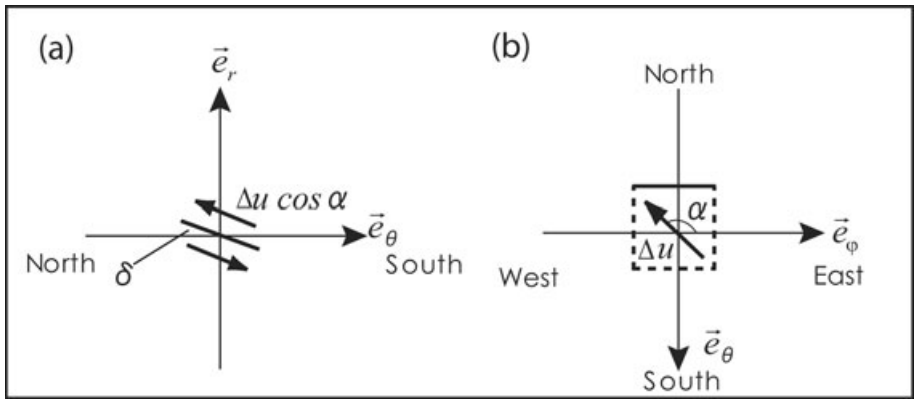

Figure 4. Definitions of the dip angle, δ, and rake angle, α. Δu denotes the applied coseismic dislocation. (a) shows a cross-section of $\varphi =$ constant. The thick solid line denotes the fault. Δu is positive when the upper plane of the fault moves northwards. (b) A plan view, where the edges of the fault are marked by the solid and dashed lines. The solid line corresponds to the most shallow edge. The slip vector on the upper plane of the fault is shown. The rake angle is measured on the fault. The strike angle is 90° (eastward; see also Fig. 6).

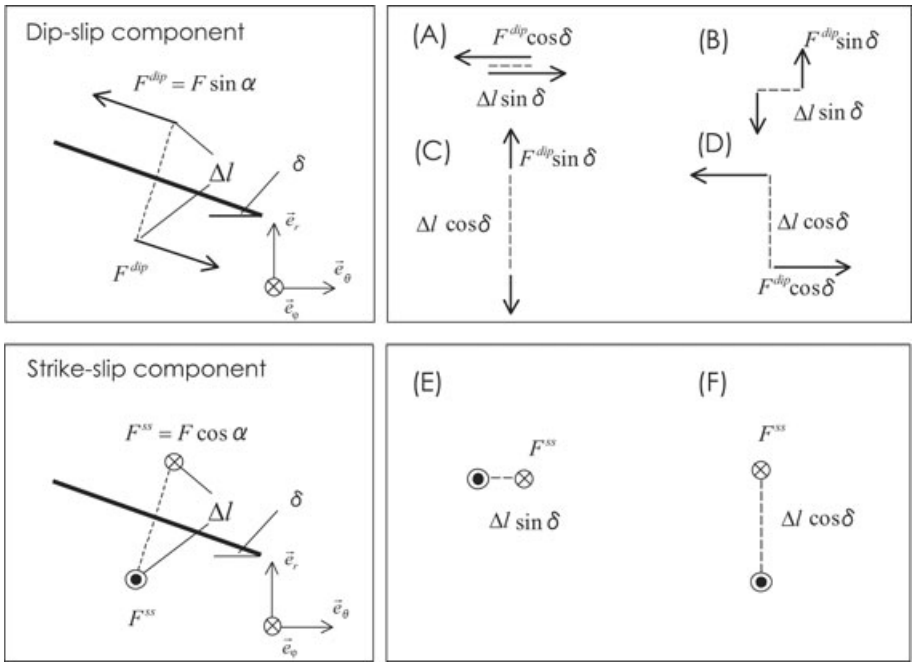

Figure 5. Partition of the single-couple forces equivalent to a shear dislocation shown in Fig. 4 into $\mathbf{e}_r$ and $\mathbf{e}_\theta$ components, representing the spheroidal part (dip-slip, a, b, c, d), and $\mathbf{e}_\varphi$ components, representing the toroidal part (strike-slip, e, f). Angles δ and α correspond to those in Fig. 4. Δl in the left-hand boxes denotes the moment arm length. $\cos\delta$ and $\sin\delta$ after Δl in the right-hand boxes are factors to account for the contribution from each type of the single-couple forces to the moment magnitude. The conjugate single-couple forces are not shown.

$$\delta\mathcal{W}^{(C-)} = -\frac{\mu_k \Delta u \Delta S}{r_0} \sin 2\delta \sin\alpha \frac{r_k}{r_{k+1} - r_{k-1}} \left(\frac{r_k}{r_{k-1}}\right) \sum_{j,m} Y_{jm}(\theta,\varphi)|_{\theta_0,\varphi_0} \delta U_{jm}^{k-1}, \tag{62}$$

$$\delta\mathcal{W}^{(D+)} = -\frac{\mu_k \Delta u \Delta S}{r_0} \cos 2\delta \sin\alpha \frac{r_k}{r_{k+1} - r_{k-1}} \left(\frac{r_k}{r_{k+1}}\right) \sum_{j,m} \left[\frac{\partial Y_{jm}^*(\theta,\varphi)}{\partial\theta}\right]_{\theta_0,\varphi_0} \delta V_{jm}^{k+1}, \tag{63}$$

$$\delta\mathcal{W}^{(D-)} = \frac{\mu_k \Delta u \Delta S}{r_0} \cos 2\delta \sin\alpha \frac{r_k}{r_{k+1} - r_{k-1}} \left(\frac{r_k}{r_{k-1}}\right) \sum_{j,m} \left[\frac{\partial Y_{jm}^*(\theta,\varphi)}{\partial\theta}\right]_{\theta_0,\varphi_0} \delta V_{jm}^{k-1}, \tag{64}$$

$$\delta\mathcal{W}^{(AT)} = \frac{\mu_k \Delta u \Delta S}{r_0} \sin 2\delta \sin\alpha \sum_{j,m} \left[\frac{\partial}{\partial\theta}\left(\frac{1}{\sin\theta}\frac{\partial Y_{jm}^*(\theta,\varphi)}{\partial\varphi}\right)\right]_{\theta_0,\varphi_0} \delta W_{jm}^{k}, \tag{65}$$

$$\delta\mathcal{W}^{(D+T)} = \frac{\mu_k \Delta u \Delta S}{r_0} \cos 2\delta \sin\alpha \frac{r_k}{r_{k+1} - r_{k-1}} \left(\frac{r_k}{r_{k+1}}\right) \sum_{j,m} \left[\frac{1}{\sin\theta}\frac{\partial Y_{jm}^*(\theta,\varphi)}{\partial\varphi}\right]_{\theta_0,\varphi_0} \delta W_{jm}^{k+1}, \tag{66}$$

$$\delta\mathcal{W}^{(D-T)} = -\frac{\mu_k \Delta u \Delta S}{r_0} \cos 2\delta \sin\alpha \frac{r_k}{r_{k+1} - r_{k-1}} \left(\frac{r_k}{r_{k-1}}\right) \sum_{j,m} \left[\frac{1}{\sin\theta}\frac{\partial Y_{jm}^*(\theta,\varphi)}{\partial\varphi}\right]_{\theta_0,\varphi_0} \delta W_{jm}^{k-1}. \tag{67}$$

Here, $\sin\alpha$ is included to account for the effect of the rake angle, and the labels (A), (B), ... , $(D\pm)$ of $\delta\mathcal{W}$ correspond to the types of single-couple forces depicted in Fig. 5. The T in the labels (AT), etc. denotes that the variation of the work is associated with the toroidal displacement, δW_{jm}.

Figs 5 (E) and (F), on the other hand, show two types of single-couple forces that are responsible for a strike-slip dislocation. The expression for type Fig. 5(E) is given by eqs. (39) and (40), whereas the variation for Fig. 5(F) can be derived in the same manner as in case of Fig. 5(B). Considering the geometrical effect of the dip and rake angles, the toroidal components of the variation of the work can be written as

$$\delta\mathcal{W}^{(ET)} = \frac{\mu_k \Delta u \Delta A}{r_0} \sin\delta \cos\alpha \sum_{j,m} \left[\frac{\partial^2 Y_{jm}^*(\theta,\varphi)}{\partial\theta^2} - \frac{1}{\sin^2\theta}\frac{\partial^2 Y_{jm}^*(\theta,\varphi)}{\partial\varphi^2}\right]_{\theta_0,\varphi_0} \delta W_{jm}^{k}, \tag{68}$$

$$\delta\mathcal{W}^{(F+T)} = \frac{\mu_k \Delta u \Delta A}{r_0} \cos\delta \cos\alpha \frac{r_k}{r_{k+1} - r_{k-1}} \left(\frac{r_k}{r_{k+1}}\right) \sum_{j,m} \left[\frac{\partial Y_{jm}^*(\theta,\varphi)}{\partial\theta}\right]_{\theta_0,.,\varphi_0} \delta W_{jm}^{k+1}, \tag{69}$$

$$\delta \mathcal{W}^{(F-T)} = -\frac{\mu_k \Delta u \Delta A}{r_0} \cos\delta \cos\alpha \frac{r_k}{r_{k+1} - r_{k-1}} \left(\frac{r_k}{r_{k-1}}\right) \sum_{j,m} \left[\frac{\partial Y^*_{jm}(\theta,\varphi)}{\partial \theta}\right]_{\theta_0,\varphi_0} \delta W^{k-1}_{jm}, \tag{70}$$

$$\delta \mathcal{W}^{(E)} = \frac{\mu_k \Delta u \Delta A}{r_0} \sin\delta \cos\alpha \sum_{j,m} \left[\frac{1}{\sin\theta} \frac{\partial^2 Y^*_{jm}(\theta,\varphi)}{\partial\theta\partial\varphi} + \frac{\partial}{\partial\theta}\left(\frac{1}{\sin\theta}\frac{\partial Y^*_{jm}(\theta,\varphi)}{\partial\varphi}\right)\right]_{\theta_0,\varphi_0} \delta V^k_{jm}, \tag{71}$$

$$\delta \mathcal{W}^{(F+)} = \frac{\mu_k \Delta u \Delta A}{r_0} \cos\delta \cos\alpha \frac{r_k}{r_{k+1} - r_{k-1}} \left(\frac{r_k}{r_{k+1}}\right) \sum_{j,m} \left[\frac{1}{\sin\theta} \frac{\partial Y^*_{jm}(\theta,\varphi)}{\partial \varphi}\right]_{\theta_0,\varphi_0} \delta V^{k+1}_{jm}, \tag{72}$$

$$\delta \mathcal{W}^{(F-)} = -\frac{\mu_k \Delta u \Delta A}{r_0} \cos\delta \cos\alpha \frac{r_k}{r_{k+1} - r_{k-1}} \left(\frac{r_k}{r_{k-1}}\right) \sum_{j,m} \left[\frac{1}{\sin\theta} \frac{\partial Y^*_{jm}(\theta,\varphi)}{\partial \varphi}\right]_{\theta_0,\varphi_0} \delta V^{k-1}_{jm}. \tag{73}$$

Thus, the expressions for the boundary conditions for a shear fault along a latitude line have been obtained (eqs 59–73).

2.3.4 Consideration for strike angle

So far, we have derived source conditions for an infinitesimal fault along the direction of $\mathbf{e}_\varphi$. In this section, we derive boundary conditions for a shear fault with an arbitrary strike angle, Θ. As in the previous section, we assume that a prescribed slip has both dip- and strike-slip components on an inclined fault ($\delta \neq \frac{\pi}{2}$). The derivation is done in a similar manner to the cases for $\Theta = 90^\circ$. The following five steps, which are summarized in Table 1, are carried out for each type of single-couple forces in Fig. 5.

Step (1): A single force with a unit magnitude **f** whose direction is parallel to a prescribed dislocation is considered. The three components of the unit direction vector shown in Table 1 are substituted into eq. (30). The relationship between the horizontal components of the single force and strike angle, Θ, is illustrated in Fig. 6.

Step (2): By differentiating the representation of the single force obtained in step (1) in the direction perpendicular to the dislocation, the corresponding single-couple forces are formed. For types (A), (B) and (E), the differentiation with respect to the horizontal coordinates as $(\sin\Theta \frac{\partial}{\partial\theta} + \cos\Theta \frac{1}{\sin\theta}\frac{\partial}{\partial\varphi})$ is used. For the other types, the differentiation is represented by applying the single forces to the two different depths (Fig. 5).

Step (3): The moment magnitude caused by the single-couple forces is multiplied by the factor corresponding to each type. The first factor denotes the effect of the rake angle, the second appears only in the dip-slip component and the third reflects the variation of the moment arm length for each type (Fig. 5).

Step (4): Expressions for conjugate single-couple forces are derived. For the dip-slip components, (A–D), this is achieved by replacing the dip angle δ by $\delta + \pi/2$ and reversing the sign of the moment. For the strike-slip components, (E) and (F), the strike angle is substituted (Table 1), since the conjugate single-couple forces are on the horizontal plane.

Step (5): The obtained expressions for the single-couple forces and their conjugate single-couple forces are substituted into the equation of the variation of the work (e.g. eq. 32) and integrated with respect to the angular variables. From types (A), (D), (E) and (F), the variation in the work associated with both spheroidal and toroidal motion are derived. For types (B) and (C) related to the vertical displacement δU_{jm}, the toroidal motion does not exist.

Implementing the above five steps, the variation in the work corresponding to each type of single-couple forces classified in Fig. 5 finally becomes

$$\begin{aligned}\delta \mathcal{W}^{(A)} = &-\frac{\mu_k \Delta u \Delta A}{r_0} \sin 2\delta \sin\alpha \sum_{j,m} \left[\sin^2\Theta \frac{\partial^2 Y^*_{jm}(\theta,\varphi)}{\partial\theta^2} + \sin\Theta\cos\Theta \left\{\frac{\partial}{\partial\theta}\left[\frac{1}{\sin\theta}\frac{\partial Y^*_{jm}(\theta,\varphi)}{\partial\varphi}\right]\right.\right. \\ &\left.\left. + \frac{1}{\sin\theta}\frac{\partial^2 Y^*_{jm}(\theta,\varphi)}{\partial\theta\partial\varphi}\right\} + \cos^2\Theta \frac{1}{\sin^2\theta}\frac{\partial^2 Y^*_{jm}(\theta,\varphi)}{\partial\varphi^2}\right]_{\theta_0,\varphi_0} \delta V^k_{jm},\end{aligned} \tag{74}$$

$$\begin{aligned}\delta \mathcal{W}^{(AT)} = &\frac{\mu_k \Delta u \Delta A}{r_0} \sin 2\delta \sin\alpha \sum_{j,m} \left\{\sin^2\Theta \frac{\partial}{\partial\theta}\left[\frac{1}{\sin\theta}\frac{\partial Y^*_{jm}(\theta,\varphi)}{\partial\varphi}\right] + \sin\Theta\cos\Theta \right. \\ &\left. \times \left[-\frac{\partial^2 Y^*_{jm}(\theta,\varphi)}{\partial\theta^2} + \frac{1}{\sin^2\theta}\frac{\partial^2 Y^*_{jm}(\theta,\varphi)}{\partial\varphi^2}\right] - \cos^2\Theta \frac{1}{\sin\theta}\frac{\partial^2 Y^*_{jm}(\theta,\varphi)}{\partial\theta\partial\varphi}\right\}_{\theta_0,\varphi_0} \delta W^k_{jm},\end{aligned} \tag{75}$$

$$\delta \mathcal{W}^{(B)} = -\frac{\mu_k \Delta u \Delta A}{r_0} \cos 2\delta \sin\alpha \sum_{j,m} \left[\sin\Theta \frac{\partial Y^*_{jm}(\theta,\varphi)}{\partial\theta} + \cos\Theta \frac{1}{\sin\theta}\frac{\partial Y^*_{jm}(\theta,\varphi)}{\partial\varphi}\right]_{\theta_0,\varphi_0} \delta U^k_{jm}, \tag{76}$$

$$\delta \mathcal{W}^{(C+)} = \frac{\mu_k \Delta u \Delta A}{r_0} \sin 2\delta \sin\alpha \frac{r_k}{r_{k+1} - r_{k-1}} \left(\frac{r_k}{r_{k+1}}\right) \sum_{j,m} Y_{jm}(\theta,\varphi)^*|_{\theta_0,\varphi_0} \delta U^{k+1}_{jm}, \tag{77}$$

Table 1. The procedure to derive source conditions for each dislocation type in Fig. 5.

Step	Explanation	(A)	(B)	(C)	(D)	(E)	(F)
(1)	Direction of single force $\mathbf{f}$, $(\nu_r, \nu_\theta, \nu_\varphi)$	$(0, -\sin\Theta, -\cos\Theta)$	$(1, 0, 0)$	$(1, 0, 0)$	$(0, -\sin\Theta, -\cos\Theta)$	$(0, -\cos\Theta, \sin\Theta)$	$(0, -\cos\Theta, \sin\Theta)$
(2)	Form of single-couple forces	$(\sin\Theta\frac{\partial}{\partial\theta} + \cos\Theta\frac{1}{\sin\theta}\frac{\partial}{\partial\varphi})\mathbf{f}$	$(\sin\Theta\frac{\partial}{\partial\theta} + \cos\Theta\frac{1}{\sin\theta}\frac{\partial}{\partial\varphi})\mathbf{f}$	$\frac{\pm\mathbf{f}}{(r_{k+1}-r_{k-1})}(\frac{r_k}{r_{k\pm1}})$	$\frac{\pm\mathbf{f}}{(r_{k+1}-r_{k-1})}(\frac{r_k}{r_{k\pm1}})$	$(\sin\Theta\frac{\partial}{\partial\theta} + \cos\Theta\frac{1}{\sin\theta}\frac{\partial}{\partial\varphi})\mathbf{f}$	$\frac{\pm\mathbf{f}}{(r_{k+1}-r_{k-1})}(\frac{r_k}{r_{k\pm1}})$
(3)	Factor to adjust moment magnitude	$\sin\alpha\cos\delta\sin\delta$	$\sin\alpha\sin^2\delta$	$\sin\alpha\sin\delta\cos\delta$	$\sin\alpha\cos^2\delta$	$\cos\alpha\sin\delta$	$\cos\alpha\cos\delta$
(4)	Conjugate single-couple forces	$\delta \to \delta + \frac{\pi}{2}, \quad \mathbf{f} \to -\mathbf{f}$		$\delta \to \delta + \frac{\pi}{2}, \quad \mathbf{f} \to -\mathbf{f}$		$\Theta \to \Theta + \frac{\pi}{2}, \quad \mathbf{f} \to -\mathbf{f}$	
(5)	Variation of the work applied	$\delta\mathcal{W}^{(\mathrm{A})}$ to $\delta\, V^k_{jm}$	$\delta\mathcal{W}^{(\mathrm{B})}$ to $\delta\, U^k_{jm}$	$\delta\mathcal{W}^{(\mathrm{C}\pm)}$ to $\delta\, U^{k\pm1}_{jm}$	$\delta\mathcal{W}^{(\mathrm{D}\pm)}$ to $\delta\, V^{k\pm1}_{jm}$	$\delta\mathcal{W}^{(\mathrm{E})}$ to $\delta\, V^k_{jm}$	$\delta\mathcal{W}^{(\mathrm{F}\pm)}$ to $\delta\, V^{k\pm1}_{jm}$
		$\delta\mathcal{W}^{(\mathrm{AT})}$ to $\delta\, W^k_{jm}$	–	–	$\delta\mathcal{W}^{(\mathrm{D}\pm\mathrm{T})}$ to $\delta\, W^{k\pm1}_{jm}$	$\delta\mathcal{W}^{(\mathrm{ET})}$ to $\delta\, W^k_{jm}$	$\delta\mathcal{W}^{(\mathrm{F}\pm\mathrm{T})}$ to $\delta\, W^{k\pm1}_{jm}$

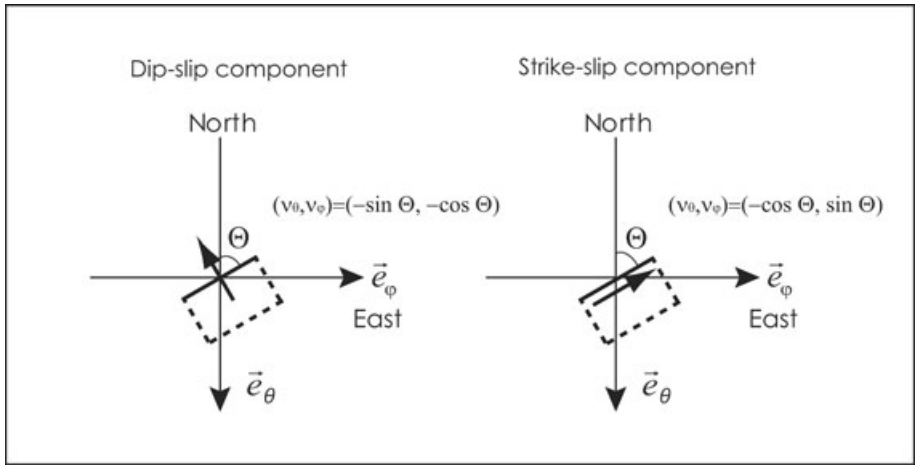

Figure 6. The relationship between the strike angle, Θ, and the horizontal components of the unit direction vector of a single force, $(\nu_\theta, \nu_\varphi)$.

$$\delta W^{(C-)} = -\frac{\mu_k \Delta u \Delta A}{r_0} \sin 2\delta \sin\alpha \frac{r_k}{r_{k+1}-r_{k-1}} \left(\frac{r_k}{r_{k-1}}\right) \sum_{j,m} Y_{jm}(\theta,\varphi)|_{\theta_0,\varphi_0} \delta U_{jm}^{k-1}, \tag{78}$$

$$\delta W^{(D+)} = -\frac{\mu_k \Delta u \Delta A}{r_0} \cos 2\delta \sin\alpha \frac{r_k}{r_{k+1}-r_{k-1}} \left(\frac{r_k}{r_{k+1}}\right) \sum_{j,m} \left[\sin\Theta \frac{\partial Y_{jm}^*(\theta,\varphi)}{\partial\theta} + \cos\Theta \frac{1}{\sin\theta} \frac{\partial Y_{jm}^*(\theta,\varphi)}{\partial\varphi} \right]_{\theta_0,\varphi_0} \delta V_{jm}^{k+1}, \tag{79}$$

$$\delta W^{(D-)} = \frac{\mu_k \Delta u \Delta A}{r_0} \cos 2\delta \sin\alpha \frac{r_k}{r_{k+1}-r_{k-1}} \left(\frac{r_k}{r_{k-1}}\right) \sum_{j,m} \left[\sin\Theta \frac{\partial Y_{jm}^*(\theta,\varphi)}{\partial\theta} + \cos\Theta \frac{1}{\sin\theta} \frac{\partial Y_{jm}^*(\theta,\varphi)}{\partial\varphi} \right]_{\theta_0,\varphi_0} \delta V_{jm}^{k-1}, \tag{80}$$

$$\delta W^{(D+T)} = \frac{\mu_k \Delta u \Delta A}{r_0} \cos 2\delta \sin\alpha \frac{r_k}{r_{k+1}-r_{k-1}} \left(\frac{r_k}{r_{k+1}}\right) \sum_{j,m} \left[\sin\Theta \frac{1}{\sin\theta} \frac{\partial Y_{jm}^*(\theta,\varphi)}{\partial\varphi} - \cos\Theta \frac{\partial Y_{jm}^*(\theta,\varphi)}{\partial\theta} \right]_{\theta_0,\varphi_0} \delta W_{jm}^{k+1}, \tag{81}$$

$$\delta W^{(D-T)} = -\frac{\mu_k \Delta u \Delta A}{r_0} \cos 2\delta \sin\alpha \frac{r_k}{r_{k+1}-r_{k-1}} \left(\frac{r_k}{r_{k-1}}\right) \sum_{j,m} \left[\sin\Theta \frac{1}{\sin\theta} \frac{\partial Y_{jm}^*(\theta,\varphi)}{\partial\varphi} - \cos\Theta \frac{\partial Y_{jm}^*(\theta,\varphi)}{\partial\theta} \right]_{\theta_0,\varphi_0} \delta W_{jm}^{k-1}. \tag{82}$$

$$\begin{aligned}\delta W^{(E)} = \frac{\mu_k \Delta u \Delta A}{r_0} \sin\delta \cos\alpha \sum_{j,m} \Bigg\{ & (\sin^2\Theta - \cos^2\Theta) \frac{1}{\sin\theta} \frac{\partial^2 Y_{jm}^*(\theta,\varphi)}{\partial\theta\partial\varphi} \\ & + (\sin^2\Theta - \cos^2\Theta) \frac{\partial}{\partial\theta} \left[\frac{1}{\sin\theta} \frac{\partial Y_{jm}^*(\theta,\varphi)}{\partial\varphi} \right] \\ & + 2\sin\Theta\cos\Theta \left[-\frac{\partial^2 Y_{jm}^*(\theta,\varphi)}{\partial\theta^2} + \frac{1}{\sin^2\theta} \frac{\partial^2 Y_{jm}^*(\theta,\varphi)}{\partial\varphi^2} \right] \Bigg\}_{\theta_0,\varphi_0} \delta V_{jm}^k,\end{aligned} \tag{83}$$

$$\begin{aligned}\delta W^{(ET)} = \frac{\mu_k \Delta u \Delta A}{r_0} \sin\delta \cos\alpha \sum_{j,m} \Bigg[& (\sin^2\Theta - \cos^2\Theta) \frac{\partial^2 Y_{jm}^*(\theta,\varphi)}{\partial\theta^2} \\ & + (\cos^2\Theta - \sin^2\Theta) \frac{1}{\sin^2\theta} \frac{\partial^2 Y_{jm}^*(\theta,\varphi)}{\partial\varphi^2} + 2\sin\Theta\cos\Theta \\ & \times \left\{ \frac{\partial}{\partial\theta} \left[\frac{1}{\sin\theta} \frac{\partial Y_{jm}^*(\theta,\varphi)}{\partial\varphi} \right] + \frac{1}{\sin\theta} \frac{\partial^2 Y_{jm}^*(\theta,\varphi)}{\partial\theta\partial\varphi} \right\} \Bigg]_{\theta_0,\varphi_0} \delta W_{jm}^k,\end{aligned} \tag{84}$$

$$\delta \mathcal{W}^{(F+)} = \frac{\mu_k \Delta u \Delta A}{r_0} \cos\delta \cos\alpha \frac{r_k}{r_{k+1} - r_{k-1}} \left(\frac{r_k}{r_{k+1}}\right) \sum_{j,m} \left[\sin\Theta \frac{1}{\sin\theta} \frac{\partial Y^*_{jm}(\theta,\varphi)}{\partial \varphi} - \cos\Theta \frac{\partial Y^*_{jm}(\theta,\varphi)}{\partial \theta} \right]_{\theta_0,\varphi_0} \delta V^{k+1}_{jm}, \tag{85}$$

$$\delta \mathcal{W}^{(F-)} = -\frac{\mu_k \Delta u \Delta A}{r_0} \cos\delta \cos\alpha \frac{r_k}{r_{k+1} - r_{k-1}} \left(\frac{r_k}{r_{k-1}}\right) \sum_{j,m} \left[\sin\Theta \frac{1}{\sin\theta} \frac{\partial Y^*_{jm}(\theta,\varphi)}{\partial \varphi} - \cos\Theta \frac{\partial Y^*_{jm}(\theta,\varphi)}{\partial \theta} \right]_{\theta_0,\varphi_0} \delta V^{k-1}_{jm}. \tag{86}$$

$$\delta \mathcal{W}^{(F+T)} = \frac{\mu_k \Delta u \Delta A}{r_0} \cos\delta \cos\alpha \frac{r_k}{r_{k+1} - r_{k-1}} \left(\frac{r_k}{r_{k+1}}\right) \sum_{j,m} \left[\sin\Theta \frac{\partial Y^*_{jm}(\theta,\varphi)}{\partial \theta} + \cos\Theta \frac{1}{\sin\theta} \frac{\partial Y^*_{jm}(\theta,\varphi)}{\partial \varphi} \right]_{\theta_0,,\varphi_0} \delta W^{k+1}_{jm}, \tag{87}$$

$$\delta \mathcal{W}^{(F-T)} = -\frac{\mu_k \Delta u \Delta A}{r_0} \cos\delta \cos\alpha \frac{r_k}{r_{k+1} - r_{k-1}} \left(\frac{r_k}{r_{k-1}}\right) \sum_{j,m} \left[\sin\Theta \frac{\partial Y^*_{jm}(\theta,\varphi)}{\partial \theta} + \cos\Theta \frac{1}{\sin\theta} \frac{\partial Y^*_{jm}(\theta,\varphi)}{\partial \varphi} \right]_{\theta_0,\varphi_0} \delta W^{k-1}_{jm}. \tag{88}$$

Thus, we have obtained the representations for the boundary conditions for a point dislocation with an arbitrary strike, dip and rake angles (eqs 74–88).

3 VALIDATION OF THE METHOD

In this section, we validate the source conditions derived in Section 2 by comparing numerical results obtained by this approach with those obtained by the method presented in Tanaka *et al.* (2006, 2007). The latter employs a numerical inverse-Laplace integration to compute viscoelastic responses to an internal dislocation for a spherically symmetric earth model. Moreover, self-gravitation and the Earth's curvature are treated rigorously. Since the approach in the current work does not transform viscoelastic responses into the Laplace domain, comparisons with results calculated by a completely different algorithm are feasible for earth models with 1-D viscosity profiles as a special case.

To compute a deformation caused by a finite fault, integrating responses to point sources is necessary on the fault plane. To eliminate errors due to this integration, we employ a point source model for the validations in Sections 3.1 and 3.2. Results for more than one point source are compared in Section 3.3.

3.1 Case (I): lower-degree gravity potential change

First, we check if variations in the lower-degree gravity potential field are computed correctly. We set the cut-off degree of spherical harmonics to 40 for computational results from both methods, corresponding to a half wavelength of 500 (=20 000/40) km, and compare variations for $j \leq 40$. The reason why we introduce such a cut-off degree is that the lower-degree gravity potential field can be observed by GRACE satellites. In analyses of GRACE data, higher-degree spherical harmonic expansion coefficients of the gravity potential field are filtered out (e.g. Gaussian) to reduce observation noises, which results in a spatial resolution of several hundred kilometres (e.g. Chen *et al.* 2007). Since we do not compare our results with observed data, we simply omit higher-degree terms instead of applying the same filter as used in the GRACE data analysis.

Fig. 7 (Left-hand panel) shows co- and postseismic geoid height changes due to a point source with a dip-slip mechanism, computed by the method presented in this study. The source is located at $(\theta, \varphi) = (90^\circ, 0^\circ)$ (i.e. colatitude and longitude = 0°). The source depth is 20 km and the dip and rake angles are 20° and 90°, respectively. A Heaviside-type source function is used. The direction of the slip is northwards on the upper plane of the fault, and the moment magnitude is 8.4 [$\Delta u = 10$ m, $\Delta A = (100\,\text{km})^2$]. The radial profile of the earth model's density, the shear modulus and the viscosity are listed in Table 2, along with the radial intervals of the 1-D grid. The density and the shear modulus are obtained by averaging the values of the PREM (Dziewonski & Anderson 1981) for five layers. The viscosity is 10^{30} Pa s within the lithosphere down to a depth of 45 km, 10^{19} Pa s between 45 and 200 km and 10^{21} Pa s between 200 km and the core–mantle boundary ($\eta^{(1)}$ in the table). The time step is 5 yr for all the computations in this study. The results in Fig. 1 are shown for up to 100 yr after the event, where the dominant viscoelastic relaxation has almost finished (note that the time interval is 50 yr between the last two contours for $t = 50$–0 and $t = 100$–0). The right-hand panel displays the profile along the line P–Q in the left-hand panel on which the result calculated by the method of Tanaka *et al.* (2006, 2007) is superimposed. The same earth model and fault parameters are used in the latter computation. We see an excellent agreement for all the time instants shown.

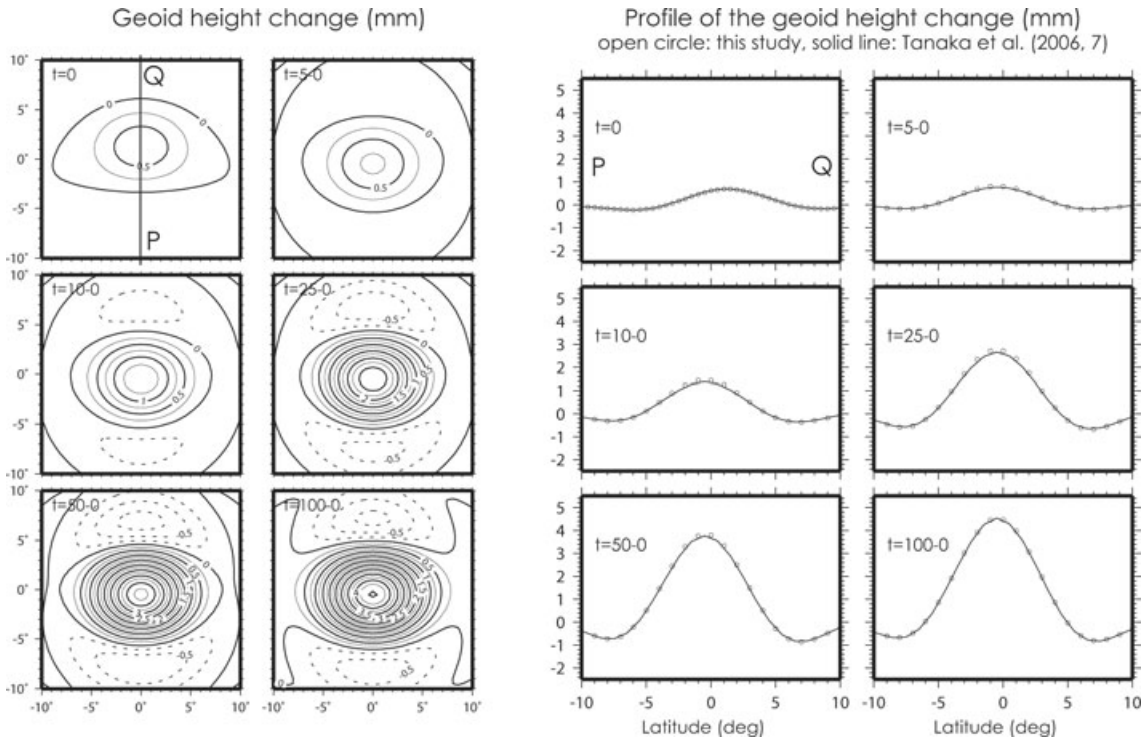

Figure 7. (Left-hand panel) The geoid height change computed for a point source with a dip-slip mechanism ($\Theta = 90^\circ, \delta = 20^\circ, \alpha = 90^\circ, M_w = 8.4$). A Heaviside-type source time function is used. The horizontal and vertical axes denote longitude and latitude in degrees, respectively. The coseismic change is marked with $t = 0$, where t is time in years. The contour interval is 0.25 mm, and the dashed lines correspond to negative values. The postseismic variation is shown in the difference from the coseismic change that occurs during the shown periods. The cut-off degree is 40. The earth model shown in Table 2 with viscosity $\eta^{(I)}$ is used. (Right-hand panel) A comparison in the profile of the geoid height change along the line P–Q in the left hand panel (longitude = 0°). The open circles represent the result obtained by the approach presented in this study, whereas the solid line shows the result obtained by the method of Tanaka *et al.* (2006) for the same model. The cut-off degree is also the same.

Table 2. The earth model parameters employed for the validation of the method described in this work. λ is used in Appendix A.

r (km)	Δr (km)	ρ (g cm^{-3})	μ (GPa)	$\eta^{(I)}$ (Pa s)	$\eta^{(II)}$ (Pa s)	λ (GPa)
0–3480	50	10.8	0	0	0	–
3480–5701	20	5.0	228	10^{21}	10^{21}	396
5701–5951	10	3.9	105	10^{21}	10^{21}	189
5951–6171	5	3.4	70	10^{21}	10^{21}	123
6171–6301	5	3.4	70	10^{19}	10^{19}	123
6301–6326	2	3.0	51	10^{19}	10^{30}	74
6326–6371	1	3.0	51	10^{30}	10^{30}	74

Fig. 8 shows co- and postseismic geoid height changes caused by a vertical strike-slip source ($\Theta = 30^\circ, \delta = 90^\circ, \alpha = 0^\circ$). Except for the strike, dip and rake angles, all the parameters are the same as those used in the verification for the dip-slip source. Again we see an excellent agreement between the results obtained by the two different methods.

3.2 Case (II): displacement field

Next, we determine if the displacement field is calculated correctly, assuming a comparison with GPS data. In contrast to Case (I), a cut-off degree is determined so that the truncation error is sufficiently small in the summation of the spherical harmonics. To reduce computational costs, however, we calculate a response to a deeper earthquake than the example shown in Case (I), since the convergence is faster for a deeper source (Sun & Okubo 1993). In the following, we set the cut-off degree to 500 for a source depth of 50 km, which corresponds to a truncation error of 1.8 per cent with respect to the case for $j_{\max} \to \infty$ (Sun & Okubo 1993). For the purpose of validating computed results, however, a truncation error does not matter, since it is common to the two approaches based on spherical harmonic expansions.

Fig. 9 shows the vertical and horizontal displacement fields due to a dip-slip point source, computed by the method presented in this study. The lithospheric thickness is 70 km and the viscosity is 10^{19} Pa s for depths between 70 and 200 km ($\eta^{(II)}$ in Table 2). The other earth model parameters and the source mechanism are the same as in the computation for the dip-slip source in Case (I). The profiles of the vertical and horizontal displacements along the lines P–Q and R–S are shown in Fig. 10, on which the results calculated by the approach of Tanaka

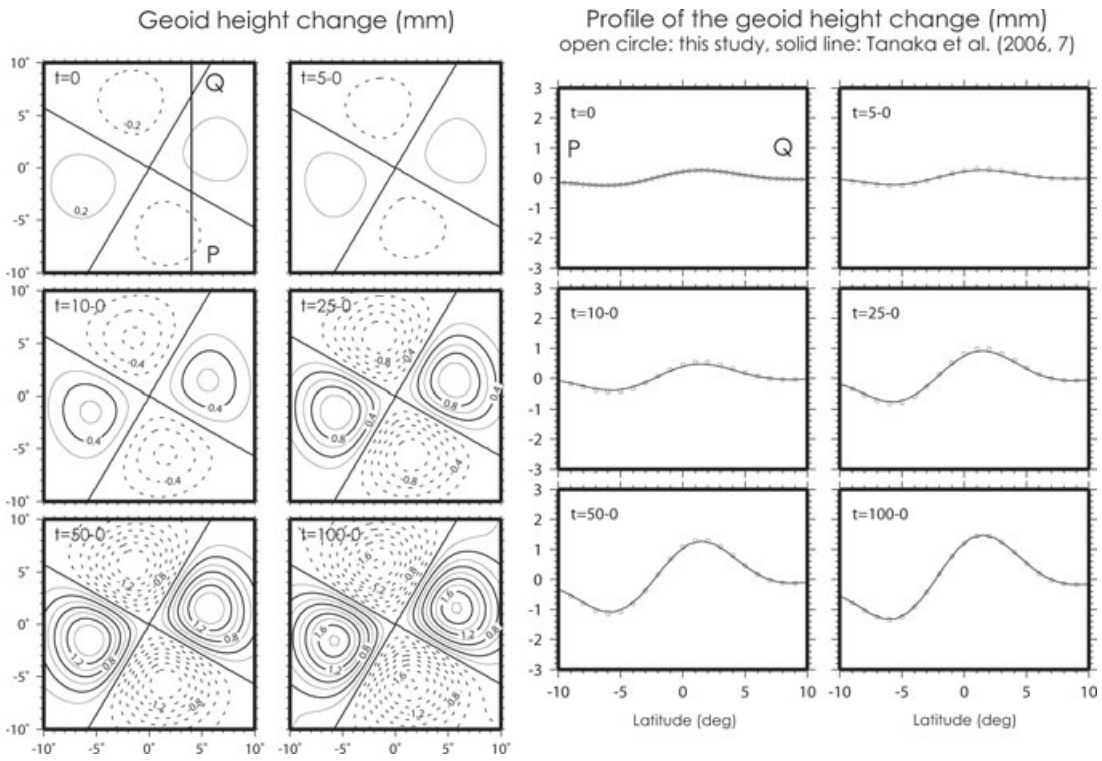

Figure 8. (Left-hand panel) The geoid height change computed for a point source with a strike-slip mechanism ($\Theta = 30^\circ, \delta = 90^\circ, \alpha = 0^\circ, M_w = 8.4$). The contour interval is 0.2 mm. (Right-hand panel) A comparison in the profile of the geoid height change along the line P–Q in the left-hand panel (longitude = 4°). See the caption of Fig. 7 for details.

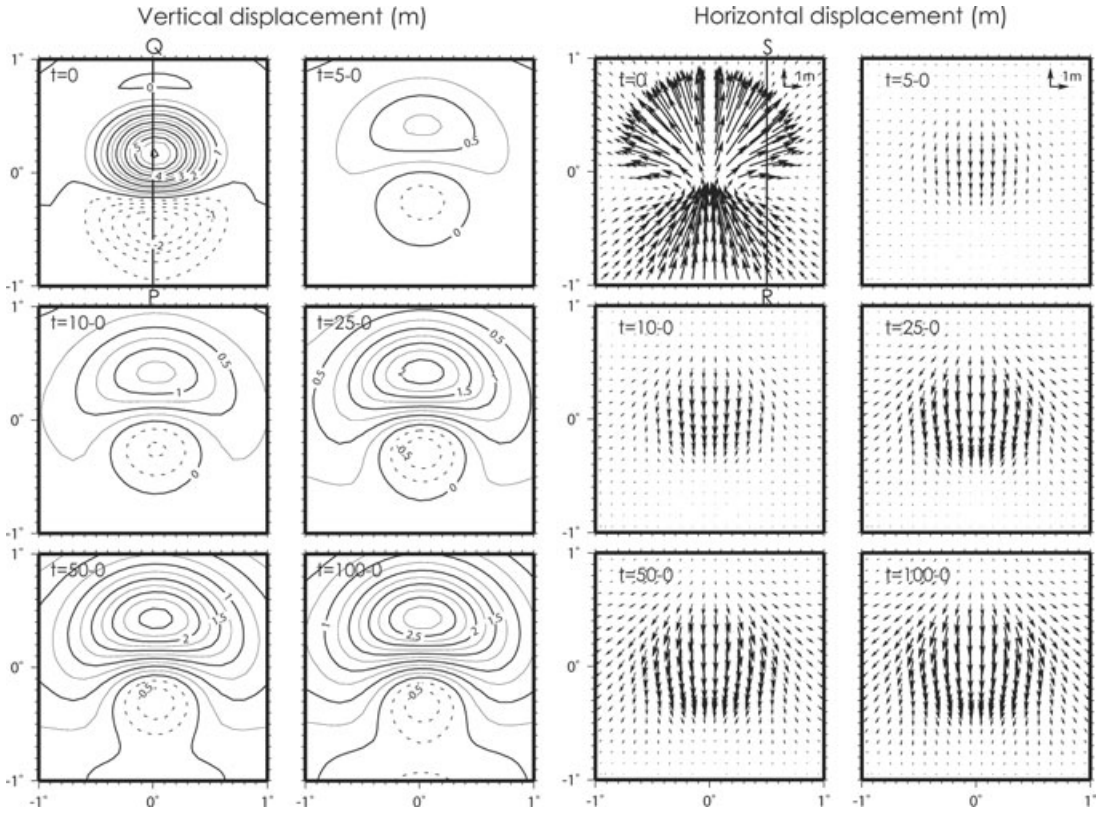

Figure 9. The surface displacement computed for a point source with a dip-slip mechanism ($\Theta = 90^\circ, \delta = 20^\circ, \alpha = 90^\circ, M_w = 8.4$). The source depth is 50 km. The contour intervals for the vertical displacement are 0.5 and 0.25 m for co- and postseismic changes, respectively. The cut-off degree is 500. The earth model shown in Table 2 with viscosity $\eta^{(II)}$ is used.

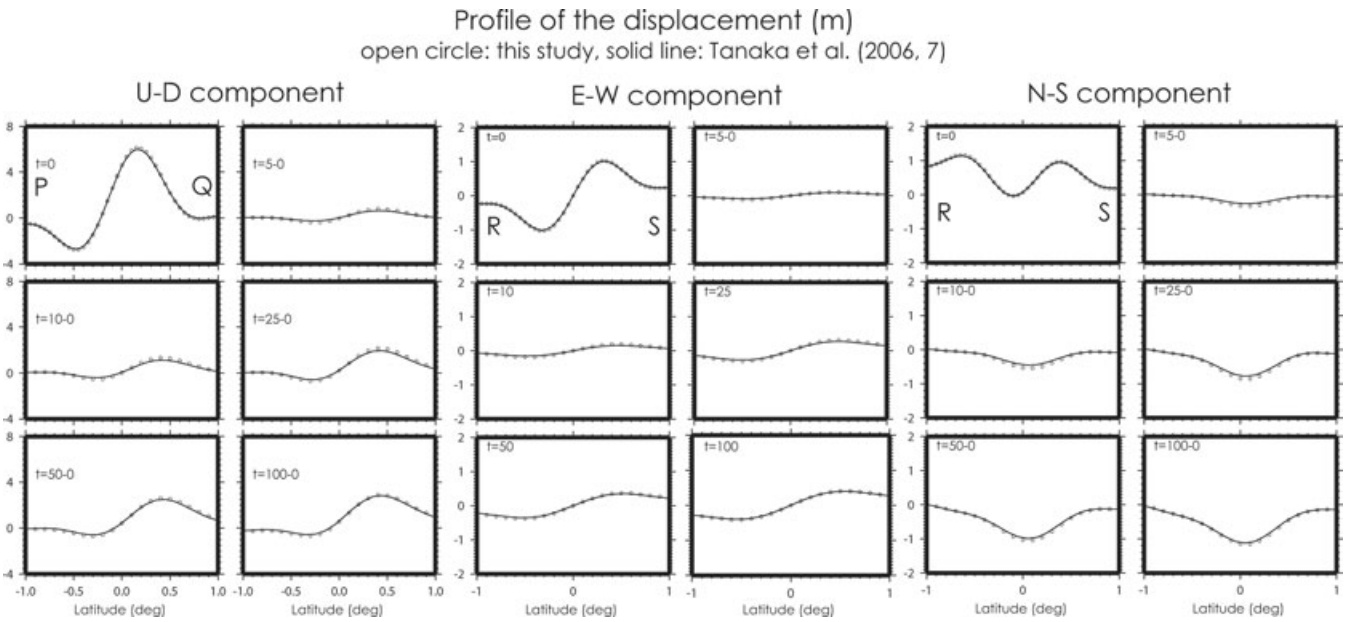

Figure 10. A comparison between the profiles of the displacement field computed with the approach presented in this study (open circles) and that computed with the method of Tanaka *et al.* (2006, 2007) (solid lines). The vertical displacement along the line P–Q in Fig. 9 (longitude $= 0^\circ$) is displayed in the left-hand panel, whereas the east–west and north–south components of the horizontal displacement along the line R–S in Fig. 9 (longitude $= 0.5^\circ$) are shown in the middle and right-hand panel, respectively.

Table 3. The earth model prameters employed for the validation of the method described in this work for the shallower earthquake.

r (km)	Δr (km)	ρ (g cm^{-3})	μ (GPa)	η (Pa s)
0–3480	50	10.8	0	0
3480–5701	40	5.0	228	10^{19}
5701–5951	5	3.9	105	10^{19}
5951–6251	2	3.4	70	10^{19}
6251–6301	0.5	3.4	70	10^{19}
6301–6326	0.5	3.0	51	10^{19}
6326–6371	0.25	3.0	51	10^{30}

et al. (2006, 2007) are superimposed. In general, the two results agree very well with each other (10 per cent at the maximum) for all the time instants shown.

3.3 Case (III): response to shallow sources distributed around the equator

Finally, we confirm if the source conditions are valid for computing a response to a finite fault. This can be achieved by putting more than one point source at different depths (D_s) and colatitudes and longitudes (θ_0 and φ_0). In addition, we check if deformation due to shallower sources is computed correctly. The latter requires a huge memory for the 3-D numerical computation since a cut-off degree to guarantee a relative accuracy of 10^{-4} for the convergence of the spherical harmonics amounts to 6000 for $D_s = 10$ km (Sun & Okubo 1993). The required memory increases approximately with $(j_{\max})^2$, and, for example, is around 20 GB for the previous case with $j_{\max} = 500$. It is therefore impossible at present to compute the responses for all degrees and orders up to 6000, even with a parallel computational environment. In this validation, therefore, we neglect dependences on the longitude ($\frac{\partial}{\partial \varphi} = 0$) and carry out a partial validation for zonal terms only.

As an example, we consider a dip-slip fault of dip angle of 20° that consists of three sources: (D_s, θ_0) = (20 km, 90°); (15 km, 89.917°) and (10 km, 89.834°). The width of each fault segment is 10 km (the total width = 30 km) and the slip is 10 m. The strike angle is the same as before. For this 2-D axisymmetric problem, the toroidal deformation W_{j0} vanishes due to a symmetry, and the deformation depends only on the epicentral distance perpendicular to the fault strike. The earth-model parameters used are listed in Table 3. In this model, the asthenosphere viscosity is set to 10^{19} Pa s. The characteristic time is approximately 10 yr.

Fig. 11 shows a comparison between the displacement field computed by the present method and that obtained by the method of Tanaka *et al.* (2006, 2007). The computation of higher-degree harmonics is implemented in the same manner as for lower-degree harmonics, and no approximations or filtering techniques are applied. Nevertheless, an excellent agreement between results is again seen. In addition, the agreement in the displacement field with a wavelength of approximately 10 km in the vicinity of the equator ($89.9^\circ < \theta < 90^\circ$) indicates that results from the presented approach are still stable for higher spherical-harmonic degrees, when using more than one source.

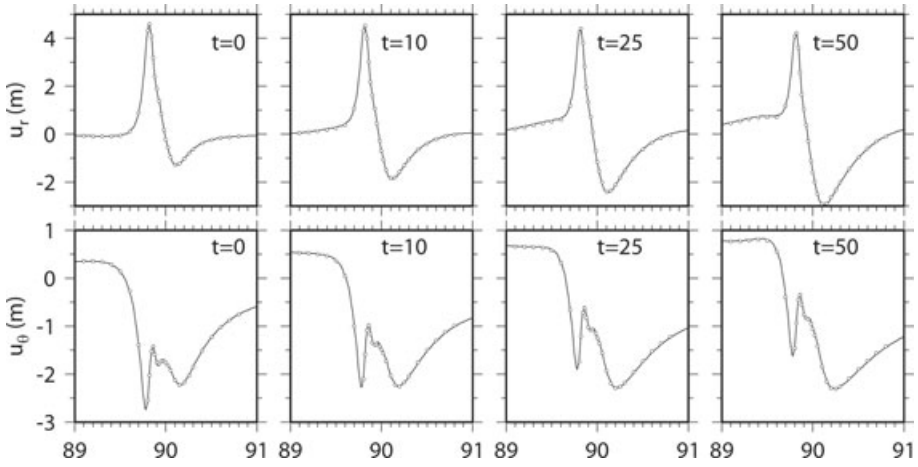

Figure 11. A comparison in the spheroidal displacement caused by a finite fault in an axisymmetric earth model. The fault model consists of three sources. Their colatitudes and source depths are described in the text. Dip angles are 20° for all sources and the fault is descending to the south. The horizontal axis denotes colatitude in degree. u_r and u_θ denote the vertical and horizontal displacements. Positive values in u_r indicate uplift. Positive values in u_θ are directed southwards. The solid lines show the result obtained by the approach applied in this study, whereas the diamonds show the results obtained by the method of Tanaka *et al.* (2006, 2007). The cut-off degree is 6000 for both approaches. Time t is given in years. The earth-model parameters are shown in Table 3.

4 INCLUSION OF A SLAB

In this section, we simulate postseismic relaxation in the presence of a slab. The source conditions that have been validated for spherically symmetric earth models are also valid for 3-D viscosity models because the term describing the effect of a 3-D viscosity structure ($\delta\mathcal{F}_{\rm diss}$ in eq. 14) is decoupled from the source term ($\delta\mathcal{W}$). The algorithm to compute this dissipation term was already validated, using an analytic solution for a special case of a 2-D problem (Martinec 2000). Therefore, to confirm if computational results for 3-D viscosity models are correct, it is sufficient to show that the obtained results converge against smaller sizes of the finite element grid (Δr), shorter time steps (Δt) and higher cut-off degrees ($j_{\rm max}$).

In the following, we apply the presented approach to three cases: the dip-slip events used in Cases (I) and (II) in the previous section and the 2004 Sumatra–Andaman earthquake.

4.1 The slab structure

Fig. 12 illustrates the viscosity structure employed for the simulation of the three events. For simplicity, an axisymmetric slab is assumed. Such a 2-D slab is employed in other studies using a finite element method (e.g. Suito & Hirahara 1999). The lateral heterogeneity in viscosity is considered in the radial interval of 6171 km $\leq r \leq$ (6371 $-$ L) km, where L denotes the lithospheric thickness. The viscosity within the lithosphere, $\eta_{\rm lith}$, is 10^{30} Pa s. The viscosity in the asthenosphere, η_1, is 10^{19} Pa s and the maximum viscosity within the slab, $\eta_{\rm slab}$, is set to 10^{23} Pa s, which is sufficiently high to account for elasticity on timescales shorter than 1000 yr. The viscosity within the slab is smoothed with a cosine function so that the viscosity on the centre line of the slab $\{\theta = \theta_c(z) \equiv 90^\circ + [(L - D_s)/\tan\delta - (L/2)/\tan\delta + z/\tan\delta]/110$, where z is a depth from the bottom of the lithosphere in km and $110 \simeq 6371 \times 2\pi/360^\circ\}$ equals $\eta_{\rm slab}$ and those at $\theta = \theta_c \pm (L/\tan\delta)/110$ become η_1 (Fig. 12). δ is the dip angle. For depths greater than 200 km, a 1-D viscosity structure is assumed (10^{21} Pa s down to the core–mantle boundary).

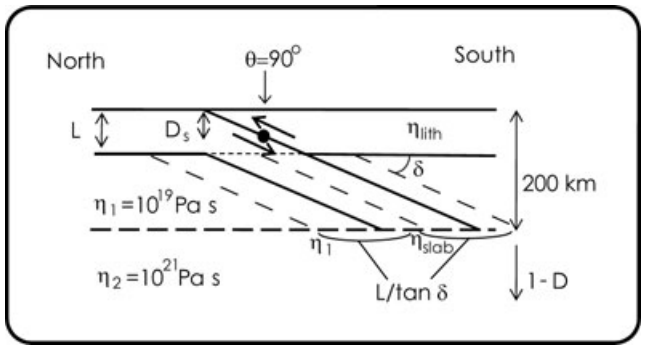

Figure 12. The viscosity structure including a 2-D slab. The slab viscosity η is smoothed with a cosine function. $\eta = 10^{23}$ Pa s on the inclined dashed line in the middle and decreases to 10^{19} Pa s on the dashed lines at both sides. For $r \leq$ 6171 km, $\eta = 10^{21}$ Pa s.

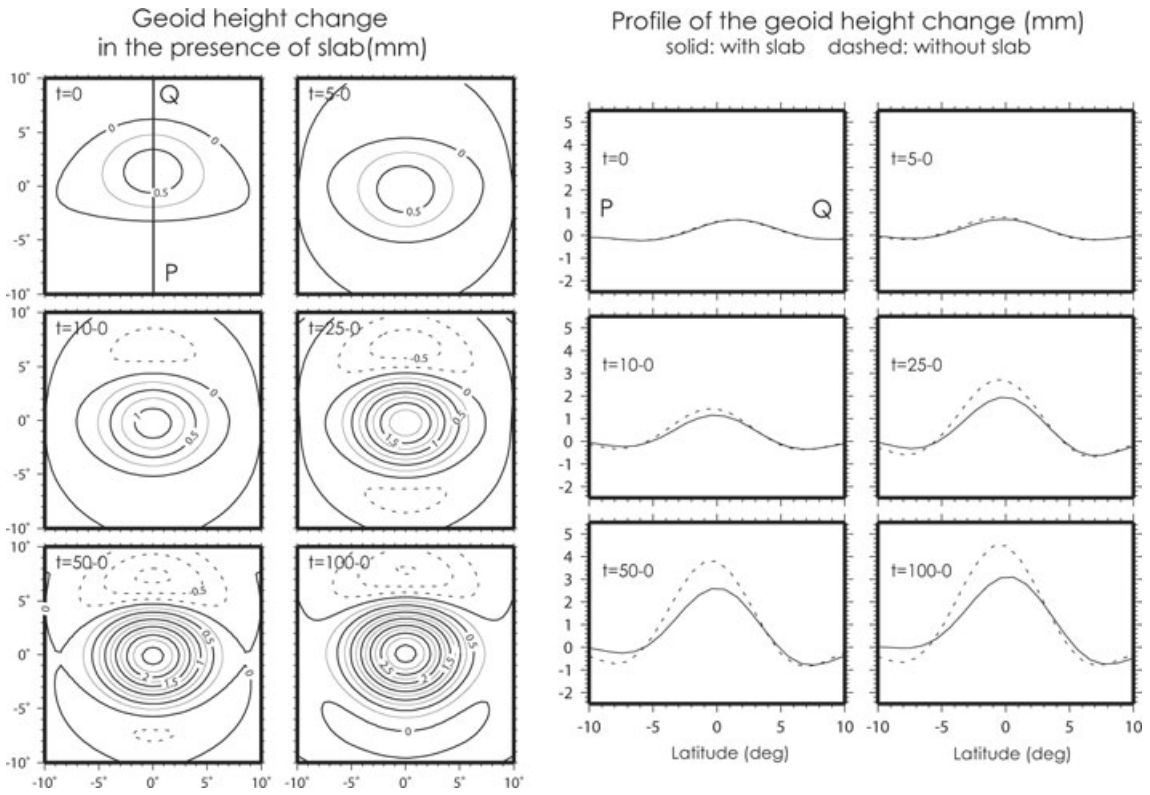

Figure 13. (Left-hand panel) The geoid height change computed for the model including the slab. The earth-model parameters and the source mechanism are the same as those used in Fig. 7, except for including the slab depicted in Fig. 12. The contour interval is 0.25 mm and the dashed lines correspond to negative values. (Right-hand panel) A comparison in the profile of the geoid height change along the line P–Q in the left-hand panel (longitude = 0°). The solid and dashed lines denote the results obtained for the model including the slab and that for the model excluding the slab, respectively.

A viscosity value in the asthenosphere should be determined so that simulated results agree with observation data. Previous studies of postseismic deformations have employed asthenosphere viscosity ranging from 10^{17} to 10^{20} Pa s (e.g. Pollitz *et al.* 2001; Fukahata *et al.* 2004; Lorenzo-Martin *et al.* 2006). In the studies of postglacial rebounds, the average mantle viscosity is considered to be around 10^{21} Pa s, which has been well constrained from comparisons with sea level changes, and so on (e.g. Peltier 1998). In general, spatial scales of postseismic deformations are smaller than those of postglacial rebounds. This implies that postseismic deformation reflects a locally low viscosity compared with the global viscosity structure. It is known that viscosity of rocks consisting of the asthenosphere becomes smaller in the presence of water (Karato 2003). The above viscosity inferred from postseismic data may be due to water supply from a subducting plate (Iwamori 2007; Kawakatsu & Watada 2007) and the existence of fluids in the lower crust (Reyners *et al.* 2007).

The viscosity beneath the lithosphere employed in this simulation (10^{19} Pa s) is a middle value of the previous cases. For a given viscosity, we will focus on differences between predicted results for models including and excluding a slab.

4.2 Application to lower-degree gravity potential changes: Case (I)

First, we compute the response to a point source to grasp the effects due to the slab. The employed earth model and the source parameters are the same as those in Section 3.1, except for including the above slab. The lithosphere thickness, L, and the source depth, D_s, are 45 and 20 km, respectively. The point source is set at $(\theta_0, \varphi_0) = (90^\circ, 0^\circ)$. The dip angle of the slab and the point source is 20°. Fig. 13 (left-hand panel) shows the geoid height change computed for the model including the slab. The coseismic change is the same as that for the model excluding the slab (Fig. 7). This is reasonable because the difference in the viscosity structure is not reflected in the elastic deformation. For $t > 0$, we see that the postseismic change becomes smaller when including the slab by approximately 30 per cent (Figs 7 and 13). In addition, we find that the difference between the two models is larger at larger colatitudes. To see this difference in more detail, we compare the profiles along the line P–Q with longitude 0° (Fig. 13; right-hand panel). Within the slab subducting to the south, the effective viscoelastic dissipation is reduced due to a higher viscosity, which results in a smaller amplitude for the surface deformation at latitudes <3°N. The difference between the two profiles increases with time and its characteristic time is similar to that for the model excluding the slab, showing that a spatial pattern is modified in the presence of the slab.

The secular variation in the geoid height change is at most 0.06 mm yr^{-1} for the model including the slab ($t = 10$–25, Fig. 13; right-hand panel). The difference in the rate caused by including the slab is 0.02 mm yr^{-1} for the first 5 yr and 0.07 mm yr^{-1} for $t = 10$–25 yr after the event at an epicentral distance of 0°, where the maximum change is expected. These rates and rate differences are below detectable signal

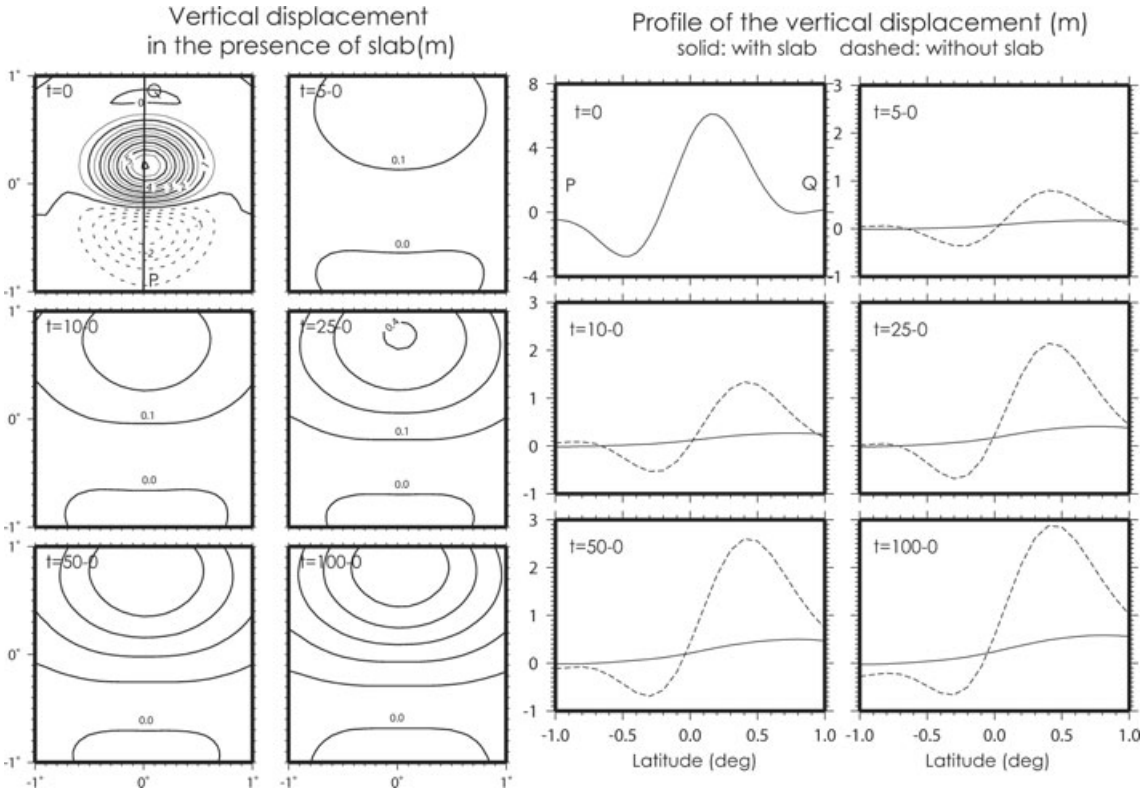

Figure 14. (Left-hand panel) The vertical displacement computed for the model including the slab. The earth model parameters and the source mechanism are the same as those used in Fig. 9, except for including the slab depicted in Fig. 12. The contour interval is 0.5 and 0.1 m for the co- and postseismic displacements, respectively, and the dashed lines correspond to negative values. (Right-hand panel) A comparison in the profile of the vertical displacement along the line P–Q in the left-hand panel (longitude = 0°). The solid and dashed lines denote the results obtained for the model including and excluding the slab, respectively.

strengths by GRACE, since differences between secular variations obtained from results published by different analysis centres amount to 0.1–0.2 mm yr^{-1} for wavelengths of several hundred kilometres.

4.3 Application to a displacement field: Case (II)

Next, we compute a postseismic displacement caused by a relatively deep event. The employed earth model and the source parameters are the same as those in Section 3.2, except for including the slab, where L and D_s are 70 and 50 km, respectively. The dip angle of the slab and the point source is 20°.

Fig. 14 (left-hand panel) shows the vertical displacement computed for the model including the slab. The coseismic change is the same as that in Fig. 9 (left-hand panel). For $t > 0$, a more drastic change is caused by the inclusion of the slab compared with the cases for the lower-degree potential field. The amplitude for the vertical deformation decreases by approximately 80 per cent, and the spatial pattern of the uplift and subsidence becomes wider in the east–west direction (Figs 9 and 14, left-hand panels), with the nodal line, on which the vertical displacement equals zero, moving towards the south by ∼0.4° at longitude 0°. Consequently, the vertical deformation changes from subsidence to uplift at epicentral distances between 0.1° and 0.5° at the continental side, where geodetic observations are carried out.

Fig. 14 (right-hand panel) shows a comparison in the profile along the line P–Q shown in the left-hand panel. In contrast to Case (I) (Fig. 13; right-hand panel), we find that the uplift at the northern side also deceases, because epicentral distances where the uplift occurs are smaller than the subducting slab width (note that the horizontal scale in Fig. 14, right-hand panel, is 1/10 of that in Fig. 13, right-hand panel). The vertical displacement rate for the model including the slab (the solid line) is 10 mm yr^{-1} for the first 5 yr, 3 mm yr^{-1} between t=10 and 25 yr and 0.2 mm yr^{-1} between t = 50 and 100 yr after the event at an epicentral distance of 0.3° S. These rates are detectable by decadal continuous GPS measurements, levelling and tide gauge observations. Excluding the slab inverts the signature of the deformation rate. The accumulated difference in the displacement caused by including the slab amounts to 0.6 m over 100 yr at an epicentral distance of 0.3° S (Fig. 14 right-hand panel). Considering the effect of a slab is important when correcting apparent vertical deformation due to postseismic relaxation at tide gauge stations for monitoring long-term sea level change (e.g. Melini *et al.* 2004).

Fig. 15 (left–hand panel) displays the horizontal displacement calculated for the model, including the slab. We see that the amplitude of the horizontal deformation decreases drastically as in the vertical deformation (note that the vector scale is different from that used in Fig. 9; right-hand panel). Moreover, spatial variations become smoother when the slab is considered. A comparison in the profile of the north–south

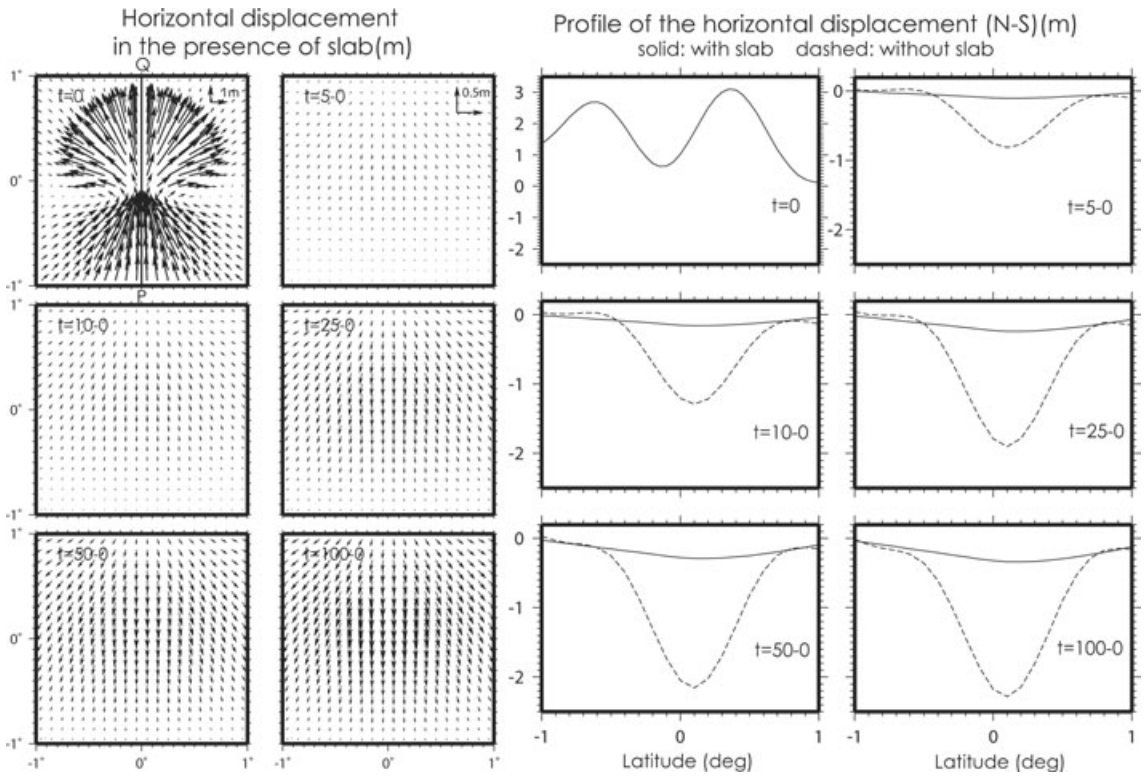

Figure 15. (Left-hand panel) The same as Fig. 14 but for the horizontal displacement. (Right-hand panel) A comparison in the profile of the north–south component of the horizontal displacement along the line P–Q (longitude = 0°; northward positive). The solid and dashed lines denote the results obtained for the model including and excluding the slab, respectively.

component at longitude 0° is shown in Fig. 15 (right-hand panel). The displacement rate is 15 mm yr^{-1} for the first 5 yr, 6 mm yr^{-1} between $t = 10$ and 25 yr and 0.4 mm yr^{-1} between $t = 50$ and 100 yr after the event at the epicentral distance of 0.3° S for the model including the slab. For $t \leq 10$, we see that the signature of the displacement rate is inverted at epicentral distances around 0.6° S. Excluding the slab increases these rates by approximately three times. For this event, the displacement rates and the rate differences due to the inclusion of the slab are detectable by continuous GPS observations.

4.4 Application to a geoid height change due to the 2004 Sumatra event

Finally, as a more realistic example, we calculate a posteismic geoid height change caused by the 2004 Sumatra earthquake, with a rectangular fault model. We construct this fault model, using the result of the seismological analysis by Yamanaka (2004; http://www.eri.u-tokyo.ac.jp/sanchu/Seismo_Note/seismo_Note/2004/EIC161a.html). The position of the fault inferred from the coseismic slip distribution is shown in the box for $t = 0$ of Fig. 16. The length and the width of the fault are 1000 and 200 km, respectively. On the fault plane, 125 point sources are placed to approximate the finite fault (5 in the dip direction $\times$25 in the strike direction). A uniform slip is assumed on the fault plane. For each point source, the slip and the area is set to 10 m and 40 km^2, so that the total moment magnitude equals 9.3. The strike, dip and rake angles are 340°, 8° and 112°, respectively. The fault slip is considered for depths between 0 and 28 km ($\simeq$200 km $\times$ tan 8°). The lithospheric thickness, L, is 30 km and $D_s = 3$, 8, 14, 20 and 25 km. The density and the elastic parameters are shown in Table 2. The slab structure is shown in Fig. 12.

Fig. 16 shows a comparison between the computational results for the model including the slab and that for the model excluding the slab. The spatial pattern of the co- and postseismic variations is modified by the strike-slip component, compared with the case for $\alpha = 90°$ (Fig. 13). Since the dip-slip component is dominant ($\alpha = 112°$), however, the effects due to the slab are similar to those seen for the point source with the purely dip-slip mechanism (Section 4.2). The horizontal scale of the slab amounts to approximately 1400 km (=200 km /tan 8°), which is larger than the half wavelength corresponding to the cut-off degree (500 km). Therefore, the postseismic gravity potential changes with wavelengths exceeding 1000 km are significantly attenuated due to the higher viscosity of the slab. On the whole, the postseismic amplitude decreases by approximately 30 per cent in the presence of the slab. The decrease is proportionally larger at the northeast side of the fault, where the slab is subducting. The decreased amplitude of the postseismic uplift over the fault due to the slab can be explained as follows. In the asthenosphere, the stress accumulation caused by the coseismic deformation is concentrated beneath the lower end of the fault. To relax this coseismic stress change, when the slab is excluded, a symmetric viscoelastic flow pattern with respect to the fault is generated in the cross-section perpendicular to the fault's strike. In other words, two flows toward the fault from far fields conflict with each other beneath the fault, which causes a mass concentration there. When the slab is included, the flow from the northeast side where the slab is subducting

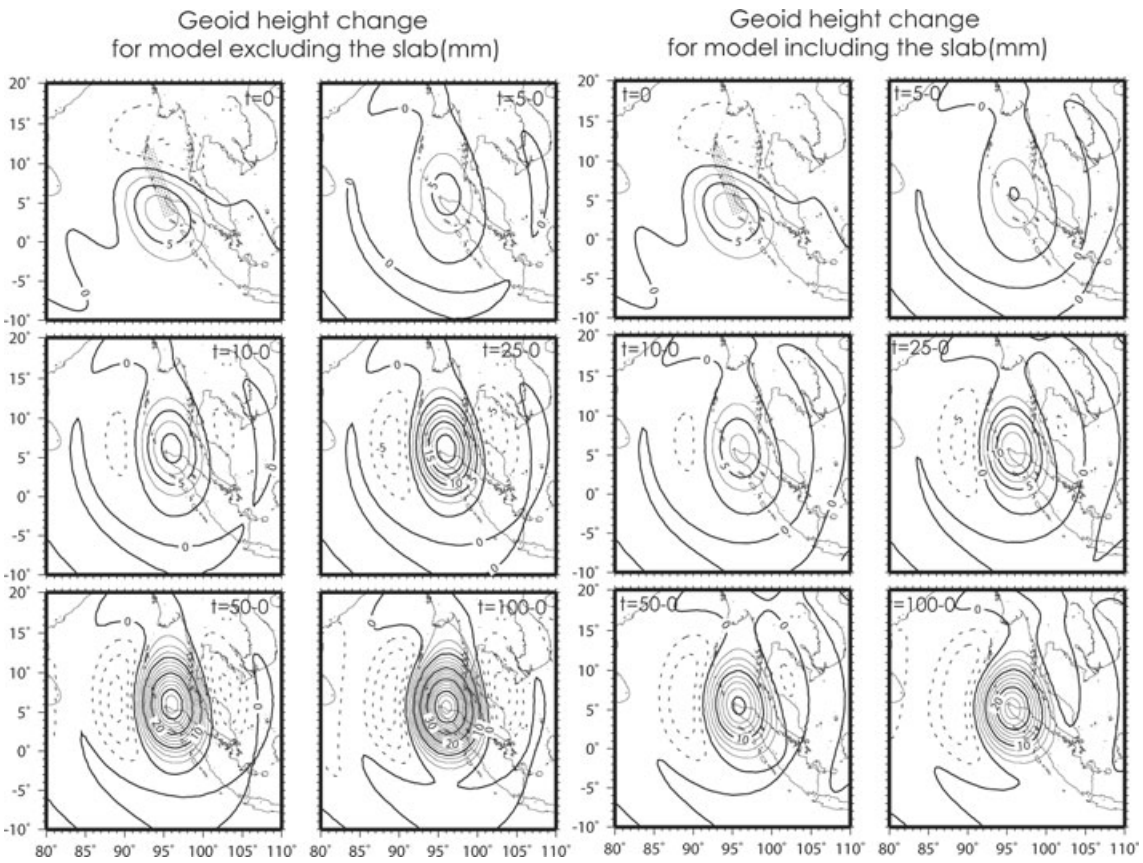

Figure 16. The geoid height changes caused by the 2004 Sumatra event computed for the model excluding (left-hand panel) and includng (right-hand panel) the slab. The contour interval is 2.5 mm. The moment magnitude is 9.3. The dots in the boxes for $t = 0$ denote the point sources used to approximate the rectangular fault.

is attenuated, which decreases the concentration of the mass, compared with the case excluding the slab. Consequently, the increase in the gravity potential over the fault becomes smaller in the presence of the slab.

The secular variation in the geoid height change expected from the model including the slab is 1 mm yr^{-1} for the first 5 yr, 0.3 mm yr^{-1} for $t = 10$–25 yr and 0.1 mm yr^{-1} for $t = 50$–100 yr after the event at the centre of the uplift. Excluding the slab overestimates the rate by approximately 40 per cent with respect to the model including the slab. From this model, we can see that effects of the slab are not negligible when interpreting short-term variations in GRACE gravity potential fields up to 5 yr after the event.

In the present model, as an example, we have taken 10^{19} Pa s for the asthenosphere viscosity to estimate the secular variation in the geoid height change. Since the relaxation time is proportional to the viscosity for a Maxwell solid, if a smaller viscosity is given as a viscosity model, the simulated rate of the geoid height change becomes larger. Some studies based on a geodetic inversion employ viscosity values lower than 10^{19} Pa s. For instance, levelling data associated with the postseismic vertical movement due to the 1946 Nankai earthquake are explained with an asthenosphere viscosity of 5×10^{18} Pa s (Fukahata *et al.* 2004). If we apply this value to our example, the deformation rate of the geoid height becomes twice as large. This implies that detecting the effects of a slab may be easier in some subduction zones having a lower viscosity.

5 DISCUSSIONS AND CONCLUSIONS

The spectral finite element approach for surface loading (Martinec 2000) has been extended to viscoelastic deformation caused by an internal dislocation. This approach enables us to consider the effects of self-gravitation, sphericity and large lateral viscosity contrasts in a rigorous way. Hence, this method is suitable for computing large-scale postseismic deformation for cases such as a subducting plate. The spectral finite-element representations of the boundary conditions are derived for a shear fault with arbitrary strike, dip and rake angles by using the equivalent double-couple forces. These representations are validated by an independent method, based on the numerical inverse Laplace integration (Tanaka *et al.* 2006, 2007) and good agreement is obtained between the computed results for 1-D viscosity models.

Using the derived source conditions, we have simulated postseismic relaxation for models including a slab. The posteismic deformation at the surface decreases at epicentral distances located above the subducting slab, since the slab's higher viscosity than in the surrounding asthenosphere hinders the effective viscoelastic dissipation. The attenuation of its amplitude is larger in the displacement field than in the gravity potential field since the spatial scale of the slab (approximately 200 km) is smaller than the resolution of the lower-degree gravity

potential field (500 km), and the lateral heterogeneity due to the slab are less reflected in the longer-wavelength deformation. The inclusion of the slab reduces the rate of the geoid height change by 30 per cent and the displacement rate by 70–80 per cent. The decrease caused by including the slab qualitatively agrees with the result of Yoshioka & Suzuki (1999), who constructed 3-D structural models, using the finite-element method without incorporating gravitational effects. The case studies show that these effects are not negligible for interpreting GRACE and GPS data, especially for large events that occur at a subduction zone with a lower viscosity.

The presented approach requires larger computational costs when calculating higher-degree terms that are needed to estimate smaller-scale deformations due to a shallower event. For an axisymmetric model, higher-degree computations are possible in a standard computational environment as shown in Section 3.3. For a 3-D model, a method should be considered to treat higher-degree terms in a computationally less expensive way. For example, it may be possible to replace higher-degree terms corresponding to sufficiently small variations compared to the lithosphere and slab by the coseismic responses computed from the method of Tanaka *et al.* (2006, 2007), since for such degrees, the excited stress does not reach the asthenosphere and the resultant postseismic relaxation can be neglected.

In this study, as a first step, we have assumed incompressibility and have shown that the spectral finite-element approach for 3-D viscosity structures is valid for modelling postseismic relaxation. Nostro *et al.* (1999), however, pointed out that the assumption of incompressibility produces a large difference in a computational result of postseismic deformation for a 2-D flat-earth model with a laterally homogeneous viscoelastic structure. Tanaka *et al.* (2007) showed that displacement rates for a spherically symmetric model differ by 10–25 per cent when considering compressibility. The question therefore arises as to which factor would be more important in modelling postseismic relaxation—the inclusion of a slab or consideration of compressibility. To confirm this, we compute a gravity variation for the dip-slip event used in Case (I), assuming a spherically symmetric and compressible earth model. The result is shown in Appendix. Both effects are of the same order of magnitude, hence both factors should be considered. To introduce compressibility into the present method for 3-D viscosity models, we should modify the constitutive equations used in this paper. A spectral representation of the constitutive equations for 1-D compressible earth models was already given in Hanyk *et al.* (1995). Therefore, we can extend this formulation into 3-D cases. The boundary conditions at a seismic source derived in this study can be used without modifications since their representations do not depend on the bulk modulus for shear dislocations. To interpret observed postseismic deformation more accurately and investigate rheology in seismogenic zones, we will continue to develop a method to take into account the effects due to compressibility.

ACKNOWLEDGMENTS

We thank Nicola Tosi, Jan Hagedoorn and Jan Bolte in GFZ for valuable discussions. This work was partially carried out while YT was visiting GFZ, supported by a scholarship from the Ministry of Education, Culture, Sports, Science and Technology, Japan. This work was also partially supported from the Grant-in-Aid for Scientific Research, Japan Society for the Promotion of Science (20840012). The research by VK was supported by the priority programme SPP 1257 of the German Research Foundation (DFG). ZM acknowledges support from the grant agency of the Czech Republic through grant No. 205/06/0580. We used the computer systems of the Earthquake Information Center of the Earthquake Research Institute, the University of Tokyo. GMT (Wessel Smith 1991) was used to draw figures in this paper.

REFERENCES

Banerjee, P., Pollitz, F.F. & Buergmann, R., 2005. The size and duration of the Sumatra–Andaman earthquake from far-field static offsets, *Science,* **308,** 1769–1772.

Bolte, J., Klotz, J., Grund, V., Moreno, M., Chen, J. & the TIPTEQ Research Group, 2007. A finite element study of the Andean Subduction Zone, *Geophys. Res. Abst.,* **9,** 02880, SRef-ID:1607-7962/gra/EGU2007-A-02880.

Boschi, E., Casarotti, E. Devotia, R., Melini, D., Piersanti A., Pietrantonio, G. & Riguzzi, F, 2006. Coseismic deformation induced by the Sumatra earthquake, *J. Geodyn.,* **42,** 52–62.

Cervelli, P., Kenner, S. & Segall, P., 1999. Correction to 'Dislocations in inhomogeneous media via a moduli perturbation approach: general formulation and two-dimensional solutions, by Du. Y, P., Segall, and H. Gao', *J. geophys. Res.,* **104,** 23 271–23 277.

Chen, J.L., Wilson, C.R., Tapley, B.D. & Grand, S., 2007. GRACE detects coseismic and postseismic deformation from the Sumatra–Andaman earthquake, *Geophys. Res. Lett.,* **34**(13), L13302, doi:10.1029/2007GL030356.

Cohen, S.C., 1994. Evaluation of the importance of model features for cyclic deformation due to dip-slip faulting, *Geophys. J. Int.,* **119**(3), 831–841.

D'Agostino, G., Spada, G. & Sabadini, R., 1997. Postglacial rebound and lateral viscosity variations: a semi-analytical approach based on a spherical model with Maxwell rheology, *Geophys. J. Int.,* **129,** F9–F13.

Dahlen, F.A., 1972. Elastic dislocation theory for a self-gravitating elastic configuration with an initial static stress field, *Geophys. J. R. astr. Soc.,* **28,** 357–383.

Dahlen, F.A., 1974. On the static deformation of an earth model with a fluid core, *Geophys. J. R. astr. Soc.,* **36,** 461–485.

Du, Y., Segall, P. & Gao, H., 1994. Dislocations in inhomogeneous media via a moduli-perturbation approach: general formulation and 2-D solutions, *J. geophys. Res.,* **99,** 13 767–13 779.

Dziewonski, A.M. & Anderson, A., 1981. Preliminary reference earth model, *Phys. Earth planet. Inter.,* **25,** 297–356.

Fu, G. & Sun, W., 2006. Global co-seismic displacements caused by the 2004 Sumatra–Andaman earthquake (M_w 9.1), *Earth Planets Space,* **58,** 149–152.

Fu, G. & Sun, W., 2007. Surface gravity changes caused by dislocations in a 3-D heterogeneous earth. *Geophys. J. Int.,* submitted.

Fu, G. & Sun, W., 2008. *Geophys. J. Int.,* **172**, 479–503.

Fukahata, Y, Nishitani, A. & Matsu'ura, M., 2004. Geodetic data inversion using ABIC to estimate slip history during one earthquake cycle with viscoelastic slip-response functions, *Geophys. J. Int.,* **156,** 140–153.

Gasperini, P. & Sabadini, R., 1989. Lateral heterogeneities in mantle viscosity and post-glacial rebound, *Geophys. J. Int.,* **98,** 413–428.

Han, S., Shum, C.K., Bevis, M., Ji, C. & Kuo, C.Y., 2006. Crustal dilatation observed by GRACE after the 2004 Sumatra–Andaman earthquake, *Science,* **313,** 658–662.

Hanyk, L., Moser, J., Yuen, D.A. & Matyska, C., 1995. Time-domain approch for the transient responses in stratified viscoelastic earth models, *Geophys. Res. Lett.,* **22,** 1285–1288.

Hu, Y., Wang, K., He, J., Klotz, J. & Khazaradze, G., 2004. Three-dimensional viscoelastic finite element model for post-seismic

deformation of the great 1960 Chile earthquake, *J. geophys. Res.,* **109,** B12403, doi:10.1029/2004JB003163.

Imanishi, Y., Sato, T., Higashi, T., Sun, W. & Okubo, W., 2004. A network of superconducting gravimeters detects submicrogal coseismic gravity changes, *Science,* **306,** 476–478.

Iwamori, H., 2007. Transportation of H_2O beneath the Japan arcs and its implications for global water circulation, *Chem. Geol.* **239,** 182–198.

Karato, S., 2003. *The Dynamic Structure of the Deep Earth, An Interdisciplinary Approach,* Princeton University Press, NJ, USA, 264 pp.

Kaufmann, G. & Wolf, D., 1999. Effects of lateral viscosity variations on postglacial rebound: an analytical approach, *Geophys. J. Int.,* **137,** 489–500.

Kaufmann, G., Wu, P. & Wolf, D., 1997. Some effects of lateral heterogeneities in the upper mantle on postglacial land uplift close to continental margins, *Geophys. J. Int.,* **127,** 175–187.

Kawakatsu, H. & Watada, S., 2007. Seismic evidence for deep water transportation in the mantle, *Science,* **316,** 1468–1471.

Klemann, V., Ivins, E., Martinec, Z. & Wolf, D., 2007. Models of active glacial isostasy roofing warm subduction: case of the south Patagonian ice field, *J. geophys. Res.,* **112,** B09405, doi:10.1029/2006JB004818.

Lorenzo-Martin, F., Roth, F. & Wang, R.J., 2006. Inversion for rheological parameters from post-seismic surface deformation associated with the 1960 Valdivia earthquake, Chile, *Geophys. J. Int.,* **164,** 75–87.

Martinec, Z., 2000. Spectral-finite element approach to three-dimensional viscoelastic relaxation in a spherical earth, *Geophys. J. Int.,* **142,** 117–141.

Melini, D., Piersanti, A., Spada, G., Soldati, G., Casarotti, E. & Boschi, E., 2004. Earthquakes and relative sealevel changes, *Geophys. Res. Lett.,* **31,** L09601, doi:10.1029/2003GL019347.

Melosh, H.J. & Raefsky, A., 1981. A simple and efficient method for introducing faults into finite element computations, *Bull. seism. Soc. Am.,* **71,** 1391–1400.

Nostro, C., Piersanti, A., Antonioli, A. & Spada, G., 1999. Spherical versus flat models of coseismic and postseismic deformations, *J. geophys. Res.,* **104,** 13 115–13 134.

Okubo, S., 1993. Reciprocity theorem to compute the static deformation due to a point dislocation buried in a spherically symmetric earth, *Geophys. J. Int.,* **115,** 921–928.

Panet, I. et al., 2007. Coseismic and postseismic signatures of the Sumatra 2004 December and 2005 March earthquakes in GRACE satellite gravity, *Geophys. J. Int.,* doi: 10.1111/j.1365-246X.2007.03525.x, **171,** 177–190.

Peltier, W.R., 1974. The impulse response of a Maxwell earth, *Rev. Geophys. Space. Phys.,* **12,** 649–669.

Peltier, W.R., 1998. Postglacial variations in the level of the sea: implications for climate dynamics and solid-earth geophysics, *Rev. Geophys.,* **36,** 603–689.

Piersanti, A., 1999. Postseismic deformation in Chile: constraints on the asthenospheric viscosity, *Geophys. Res. Lett.,* **26,** 3157–3160.

Piersanti, A., Spada, G., Sabadini, R. & Bonafede, M., 1995. Global postseismic deformation, *Geophys. J. Int.,* **120,** 544–566.

Piersanti, A., Spada, G. & Sabadini, R., 1997. Global postseismic rebound of a viscoelastic Earth: theory for finite faults and application to the 1964 Alaska earthquake, *J. geophys. Res.,* **102,** 477–492.

Pollitz, F.F., 1992. Postseismic relaxtaion theory on the spherical earth, *Bull. seism. Soc. Am.,* **82,** 422–453.

Pollitz, F.F., 1997. Gravitational viscoelastic postseismic relaxation on a layered spherical Earth, *J. geophys. Res.,* **102,** 17 921–17 941.

Pollitz, F.F., 2003. Postseismic relaxation theory on a laterally heterogeneous viscoelastic model, *Geophys. J. Int.,* **155,** 57–78.

Pollitz F.F., Wicks, C. & Thatcher, W., 2001. Mantle flow beneath a continental strike-slip fault: postseismic deformation after the 1999 Hector Mine earthquake, *Science,* **293,** 1814–1818.

Pollitz, F.F., Buergmann, R. & Banerjee, P., 2006. Postseismic relaxation following the great 2004 Sumatra–Andaman earthquake on a compressible self-gravitating Earth, *Geophys. J. Int.,* **167,** 397–420.

Reyners, M., Eberhart-Phillips, D. & Stuart, G., 2007. The role of fluids in lower-crustal earthquakes near continental rifts, *Nature,* **446,** 1075–1078.

Sabadini, R., Yuen, D.A. & Boschi, E., 1984. The effects of post-seismic motions on the moment of inertia of a stratified viscoelastic earth with an asthenosphere, *Geophys. J. R. astr. Soc.,* **79,** 727–745.

Sabadini, R., Yuen, D.A. & Portney, M., 1986. The effects of upper-mantle lateral heterogeneities on postglacial rebound, *Geophys. Res. Lett.,* **13,** 337–340.

Stein, S. & Okal, E.A., 2005. Speed and size of the Sumatra earthquake, *Nature,* **434,** 581–582.

Suito, H. & Hirahara, K., 1999. Simulation of postseismic deformations caused by the 1896 Riku-u earthquake, northeast Japan: re-evalution of the viscosity in the upper mantle, *Geophys. Res. Lett.,* **26,** 2561–2564.

Sun, W. & Okubo, S., 1993. Surface potential and gravity changes due to internal dislocations in a spherical earth I: theory for a point dislocation, *Geophys. J. Int.,* **114,** 569–592.

Sun, W., Okubo, S. & Vanicek, P., 1996. Global displacements caused by point dislocations in a realistic Earth model, *J. geophys. Res.,* **101**(B4), 8561–8577.

Takeuchi, H. & Saito, M., 1972. Seismic surface waves, *Methods Comput. Phys.,* **11,** 217–295.

Tanaka, Y., Okuno, J., & Okubo, S., 2006. A new method for the computation of global viscoelastic postseismic deformation in a realistic earth model (I): vertical displacement and gravity variation, *Geophys. J. Int.,* **164,** 273–289.

Tanaka, Y., Okuno, J., & Okubo, S., 2007. A new method for the computation of global viscoelastic post-seismic deformation in a realistic earth model (II): horizontal displacement, *Geophys. J. Int.,* doi:10.1111/j.1365-246X.2007.03486.x, **170,** 1031–1052.

Thatcher, W. & Rundle, J.B., 1979. A model for the earthquake cycle in underthrust zones, *J. geophys. Res.,* **84,** 5540–5556.

Tromp, J. & Mitrovica, J.X., 2000. Surface loading of a viscoelastic Earth, III: aspherical models, *Geophys. J. Int.,* **140,** 425–441.

Wang, H., 1999. Surface vertical displacements, potential perturbations and gravity changes of a viscoelastic earth model induced by internal point dislocations, *Geophys. J. Int.,* **137,** 429–440.

Wang, K., He, J., Dragert, H. & James, T.S., 2001. Three-dimensional viscoelastic interseismic deformation model for the Cascadia subduction zone, *Earth planets Space,* **53,** 295–306.

Wessel, P. & Smith, W.H.F., 1991. Free software helps map and display data, *EOS, Trans. Am. geophys. Un.,* **72,** 441, 445–446.

Wu, P., 2002. Mode coupling in a viscoelastic self-gravitating spherical earth induced by axisymmetric loads and lateral viscosity variations, *Earth planet. Sci. Lett.,* **202,** 49–60.

Yoshioka, S. & Suzuki, S., 1999. Effects of three-dimensional inhomogeneous viscoelastic structures on postseismic surface deformations associated with the great 1946 Nankaido earthquake, *Pure appl. Geophys.,* **154,** 307–328.

Zhao, D., Hasegawa, A. & Kanamori, H., 1994. Deep structure of Japan subduction zone as derived from local, regional and teleseismic events, *J. geophys. Res.,* **99,** 22 313–22 329.

Zhong, S., Paulson, A. & Wahr, J., 2003. Three-dimensional finite-element modelling of Earth's viscoelastic response: effects of lateral variations in lithospheric thickness, *Geophys. J. Int.,* **155,** 679–695.

APPENDIX A: EFFECTS DUE TO COMPRESSIBILITY FOR A SPHERICALLY SYMMETRIC MODEL

A method to compute postseismic gravity potential change for a spherically symmetric, self-gravitating and compressible earth model was developed in Tanaka *et al.* (2006, 2007), which is also used in this study to validate the source conditions in Section 3, for an incompressible

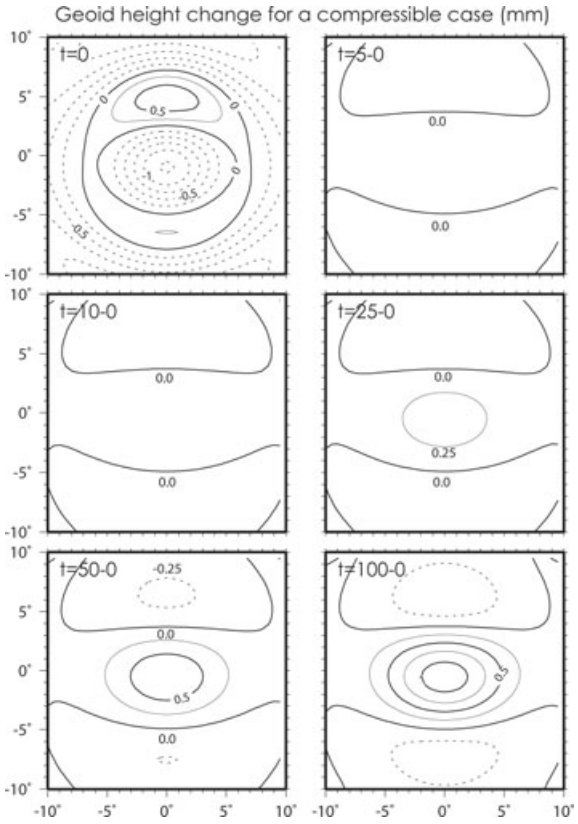

Figure A1. The geoid height change computed for a compressible earth model excluding the slab. The contour interval is 0.25 mm. The earth model parameters are shown in Table 2, including the elastic constant, λ. The source mechanism is the same as that used in Fig. 7 (Left-hand panel).

model as a special case. Using this method, we calculate a geoid height change caused by the dip-slip event used in Case (I) for a compressible model excluding the slab. The earth model parameters and the source mechanism are the same as in the incompressible case except that the elastic constant, λ, is added. The employed λ is shown in Table 2, which is based on the averaged PREM.

Fig. (A1) displays the result computed with the same cut-off degree, $j_{\max} = 40$. By comparing Fig. 7 (Left-hand panel) with this figure, we see that a large difference is caused by considering compressibility in the coseismic change. In particular, the geoid height decreases above the source and in the surrounding area, which is not seen in the incompressible case. The amplitude at the centre of the uplift, however, is almost the same (∼0.5 mm). For $t > 0$, the spatial pattern of the uplift and subsidence is similar to that for the incompressible model (the uplift in the centre surrounded by the subsidence in the north and the south). However, the amplitude of the postseismic change for the compressible case is reduced by approximately 70 per cent. For this event, the effects due to compressibility are approximately twice as large as the effects of the lateral heterogeneity in viscosity due to the slab.